Iranian Polymer Journal (2025) 34:977–999
https://doi.org/10.1007/s13726-024-01414-6

ORIGINAL RESEARCH

Polyimide synthesis and characterizations: DFT-assisted computational studies on structural units

Baris Kartal[1] · Aslihan Aycan Tanriverdi[2] · Umit Yildiko[3] · Ahmet Turan Tekes[2] · Ismail Çakmak[2]

Received: 31 May 2024 / Accepted: 23 October 2024 / Published online: 4 November 2024
© Iran Polymer and Petrochemical Institute 2024

Abstract

A diamine was obtained from commercial pyridin-4-amine through a two-step synthesis (dinitro to diamine). The final combination of diamine, disulfonic acid, and pyromellitic dianhydride resulted in poly(amic acid)$_x$ (PAA_x), and the original sulfonated polyimide$_x$ (SPI_x) was produced by polycondensation. Various characterizations of dinitro, diamine, and SPI_x were performed, with each material analyzed individually. Quantum chemical calculations of SPI_x, Density Functional Theory (DFT) studies, and innovative analyses derived from DFT output data were carefully examined. An important point is that the molecular weight of SPI_x (M_n 28,300 g.mol^{-1}) was calculated using end-group signals obtained by proton nuclear magnetic resonance (^{1}H NMR) spectra (-NH at 2.21 ppm and -NH_2 at 1.15 ppm). Similarly, to gain prior knowledge about the conductivity or insulation properties of the material, the λ_{max} value (430 nm) and band gap (Δ) (2.88 eV) in the ultraviolet–visible (UV–vis) spectrum were calculated and compared with the band gap (Δ) energy values (1.784 eV, 0.988 eV, and 1.719 eV) provided by the theoretical E_{HOMO}-E_{LUMO} calculations. Thermal thermograms suggest that the final polymer can exhibit high thermal resistance and perform well as an engineering material. The morphological properties of the polymer were clearly presented through cross-sectional scanning electron microscopy (SEM) observations, providing qualitative insights into the product's behavior under environmental stress. All these characterizations and theoretical calculations offer predictions for the future application areas of this newly synthesized polymer. Theoretical data can be used to comment on the hydration properties, proton transfer, electrical properties, and optical properties of the polymer. Our study is actually aimed at this.

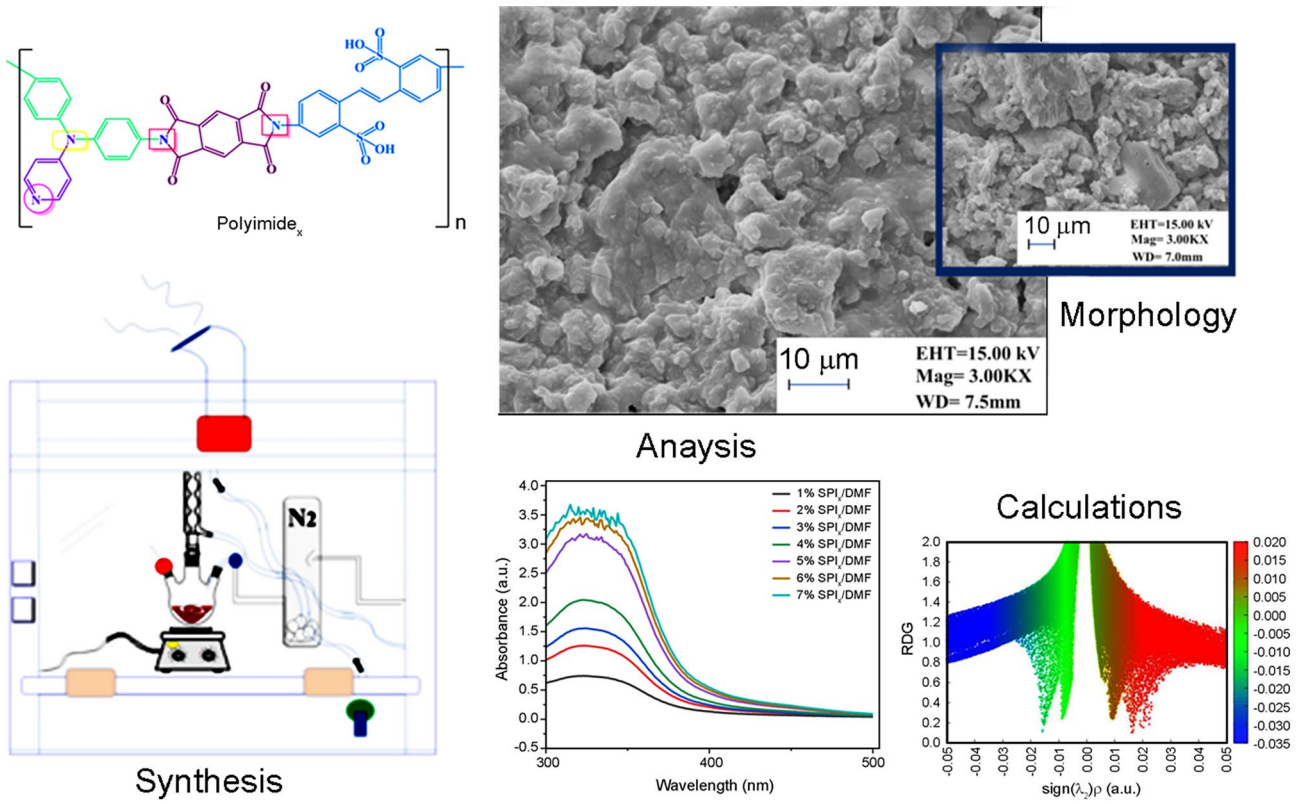
✉ Aslihan Aycan Tanriverdi
t.aslihanaycan@gmail.com

[1] Safety and Healthy Occupational, Security and Protection Property, Adiyaman University, Adıyaman 02100, Turkey

[2] Faculty of Arts and Sciences, Department of Chemistry, Kafkas University, Kars 36100, Turkey

[3] Engineering and Architecture Faculty, Department of Bioengineering, Kafkas University, Kars 36100, Turkey

Graphical abstract



Keywords Pyridin-4-amine · Sulfonated polyimide · NLO · Density functional theory · RDG · ELF

Introduction

With the rapid growth of aviation industry, there is a necessity for dynamic requirements based on new, advanced technology [1]. Unfortunately, most of these needs cannot be met with existing plastic and metal materials [2]. Brand new materials were needed that were thermally stable, oxidation-resistant, had good mechanical properties, were lightweight, and would perform well in spacebourne environments [3]. Additive manufacturing methods are expanding to various applications, including electrochemical and medical fields, using inexpensive thermoplastics, commonly used metals, composites, and hydrogels [4]. The creation of hard and soft phases in the microstructure of polymers can be achieved either through synthesis or blending [5]. Polyimides (PIs), a class of polymers, were introduced as commercial products in the early 1960s [6–8]. PIs are characterized by the presence of repeating imide structural units in the polymer backbone [9, 10]. This macromolecule greatly contributes to the outstanding oxidative and thermal stability of PIs [11]. They are generally prepared from various dianhydride and diamine monomers. The presence of the imide structure results in a polymer with high thermo-oxidative stability and a high glass transition temperature (T_g). The synthesis process involves two steps: first, preparing the intermediate poly(amic acid) (PAA) prepolymer, and second, converting the prepolymer to PI through a specific curing cycle [12–14].

Today, environmental pollution is a critical issue faced by society. New technologies are continuously being investigated to purify air, water, and soil from pollutants. Heavy metals, particulate matter, fertilizers, herbicides, pesticides, toxic gases, oil spills, industrial wastes, organic compounds, and sewage are among the many concerning pollutants. Various materials can be used in environmental cleaning, leading to a wide range of approaches. The retention and degradation of environmental pollutants are challenging due to difficulties in mixing different compounds, low reactivity, and high volatility [15, 16]. Recent studies have shown promise in using nanomaterials for advancing new environmental remediation technologies. Nanotechnology has garnered considerable attention in recent years due to the unique physical properties of nanoscale materials and high-performance polymer composites. Nanomaterials, with their high surface-to-volume ratios and improved reactivity

compared to their bulk counterparts, are more effective in pollutant removal [17, 18]. Adjusting the physical properties of nanomaterials can offer significant advantages that enhance their performance in pollutant remediation. Materials used for pollution removal should not contribute to contamination during or after use; they should be biodegradable. Consequently, recent studies have focused on utilizing nanotechnology to develop engineering materials capable of overcoming the challenges of pollutant removal. Key considerations in producing specialized nanomaterials for environmental remediation include target acquisition, easy synthesis, cost-effectiveness, non-toxicity, biodegradability, green chemistry, recyclability, and renewability after use. Thus, thorough research is required on production processes and performance optimization to develop effective nanomaterial candidates that can address environmental problems [19–21].

Theoretical data in the DFT method is used to compute local and global chemical indices. This approach, combined with the basis set of polarization functions, provides accurate descriptions of the electrical and geometrical features of the molecule under study, as well as quantum chemical computations [22–25]. In principle, DFT methods, regardless of the functional or basis set used, require reference to experimental data or at least calculations based on experimental data. In contrast, HF and post-HF methods form a convergent family, which may lead to solutions that lack significance within the framework of DFT theory. Therefore, it is essential to validate the computational setup using one or more similar complexes that contain the same metal ions and ligands, with structural data that are known and closely related to the molecule under study [26, 27]. It involves selecting oligomers of the molecule with extended π-conjugation in the presence of non-planar geometry. Theoretical research can provide microscopic explanations for both well-known and obscure features of these oligomers [28–30]. The use of DFT and quantum studies to enhance the understanding of open structures in polymer materials within a computer environment is not widely covered in the literature.

In the quantum theory of atoms in molecules (QTAIM), an atom is defined as a region that can share electron density and localized energy in space. It acts as a center that attracts electron density. Therefore, it can be described by its localizations where the electron density is concentrated [31–33]. It is a mathematical approach known in the literature as charge density topology. This method relies on the topological analysis of electron density (ρ), where the attractive forces of the nuclei are considered [34, 35]. These topological factors are $\rho(r)$ (electron density), a gradient norm of electron density ($\nabla\rho(r)$), Laplacian of electron density ($\nabla^2\rho(r)$), electron potential energy density ($V(r)$), Lagrangian kinetic energy density ($G(r)$), Hamiltonian kinetic energy density ($H(r)$) [35–37].

In this study, *N*,*N*-bis(4-nitrophenyl)pyridine-4-amine, *N*,*N*-bis(4-aminophenyl)pyridine-4-amine, and SPI_x are compounds that have not been synthesized before. Additionally, the DFT studies and QTAIM topological parameters (such as electron density, gradient norm of electron density, Laplacian of electron density, electron potential energy density, Lagrangian kinetic energy density, Hamiltonian kinetic energy density, RDG plots, and ELF topological graphs) performed on SPI_x represent innovative theoretical research. The molecular weight of the final polymer was calculated using end-group signals obtained from ^{1}H NMR spectra, in addition to classical methods. Similarly, the band gap from the UV–vis spectrum was calculated and compared with theoretical energy gap (Δ) values. In thermal characterizations, SPI_x demonstrated high thermal resistance. The morphological properties of the polymer suggest that it will exhibit the expected behavior under environmental effects. All these characterizations and theoretical calculations offer alternative and innovative predictions for the future application areas of this newly synthesized polymer.

Experimental

Materials

Pyridine-4-amine (~97%, Sigma Aldrich), cesium fluoride (CsF) (~99%, Sigma Aldrich), 1-fluoro-4-nitrobenzene ($FC_6H_4NO_2$) (~99%, Sigma Aldrich), acetic acid (≥ 99% Sigma Aldrich), dimethyl sulfoxide (DMSO) (~99%, Sigma Aldrich), ethyl alcohol (~96%, Sigma Aldrich), palladium (Pd/C) (10% by wt loading, matrix activated carbon support, Sigma Aldrich), hydrazine monohydrate (N_2H_6O) (~64–65%, Sigma Aldrich), pyromellitic dianhydride (~99.5%, Sigma Aldrich), 4,4′-diamino-2,2′-stilbenedisulfonic acid (85%, Sigma Aldrich), benzoic acid (~99.5%, Sigma Aldrich), triethylamine (~99.5%, Sigma Aldrich), *m*-Cresol (~99%, Sigma Aldrich), ethyl acetate (~99%, Sigma Aldrich), acetone (~99.5%, Sigma Aldrich) and diethyl ether (~99.5%, Riedel–de Haen), petroleum ether (~99%, Riedel–de Haen) were purchased.

Characterizations

A Heidolph MR 3001 model heated magnetic stirrer (Germany) was used in the synthesis reactions to adjust the temperature and mixing speed until polymerization occurred. The VT 6025 model Heraeus Vacutherm oven (Germany) was used for drying the obtained monomer and polymer under constant temperature and pressure. A Bruker Compact: Alpha II model Fourier-transform infrared (FTIR) spectrophotometer (Germany) was employed to partially elucidate the structure and study the chemical composition of

SPI_x using the IR spectrum of the synthesized compounds. Carbon-13 nuclear magnetic resonance (^{13}C NMR) and ^{1}H NMR spectroscopy were performed for qualitative analysis and structural determination with a Bruker Avance III HD model (United States). The UV–Vis absorption spectra of the compound were investigated using a Multiskan Sky microplate spectrophotometer (United States). Differential scanning calorimetry (DSC) analysis was conducted for the thermal analysis of polyimide 1 to determine the T_g of the polymers. Thermogravimetric analysis/differential thermal analysis (TGA/DTA) evaluations were performed in N_2 flow using a Setaram Labsys Evo (Germany) to assess thermal degradation. SEM analysis was carried out with a Zeiss EVO 10 (United States).

Simulations

Open structures were drawn using ChemDraw. The drawn molecule was then adapted to a MOL2 file in Chem3D and opened in the Gauss View interface. SPI_x structural units (oligomeric, not polymeric) were analyzed using Gaussian 09 W (revision B.01) software [38] with the 6-311G basis set for the DFT/B3LYP method and the 6-311G (d,p) basis set for the time-dependent density functional theory (TD-DFT)/B3LYP method. Calculations were initiated, resulting in LOG and chk files generated by the computer environment. Theoretical chemical calculations of SPI_x were conducted using these files, and software images were carefully obtained and presented as figures. To analyze the non-linear optical (NLO) behavior, polarity (α), static higher-order polarity (β), and electric dipole moment (μ) were determined using literature equations. The molecular electrostatic potential (MEP) of the structural units was visualized using the GaussView 6.0 program [38]. The command was then applied in Gaussian 09W to convert the chk file obtained from the DFT-B3LYP/6-311G set into a checkpoint file. Topological analysis data were obtained from the AIMAII program using the checkpoint file. The checkpoint file containing the SPI_x unit was directly transferred to the program. QTAIM study parameters such as $\rho(r)$, $\nabla\rho(r)$, $\nabla^2\rho(r)$, $H(r)$, $V(r)$, and $G(r)$ were extracted from the AIMAII program and presented as images. Similarly, the checkpoint file was converted to another formatted checkpoint file and transferred to the Multiwfn 3.8 version program to create electron localization function (ELF) graphical and reduced density gradient (RDG) images.

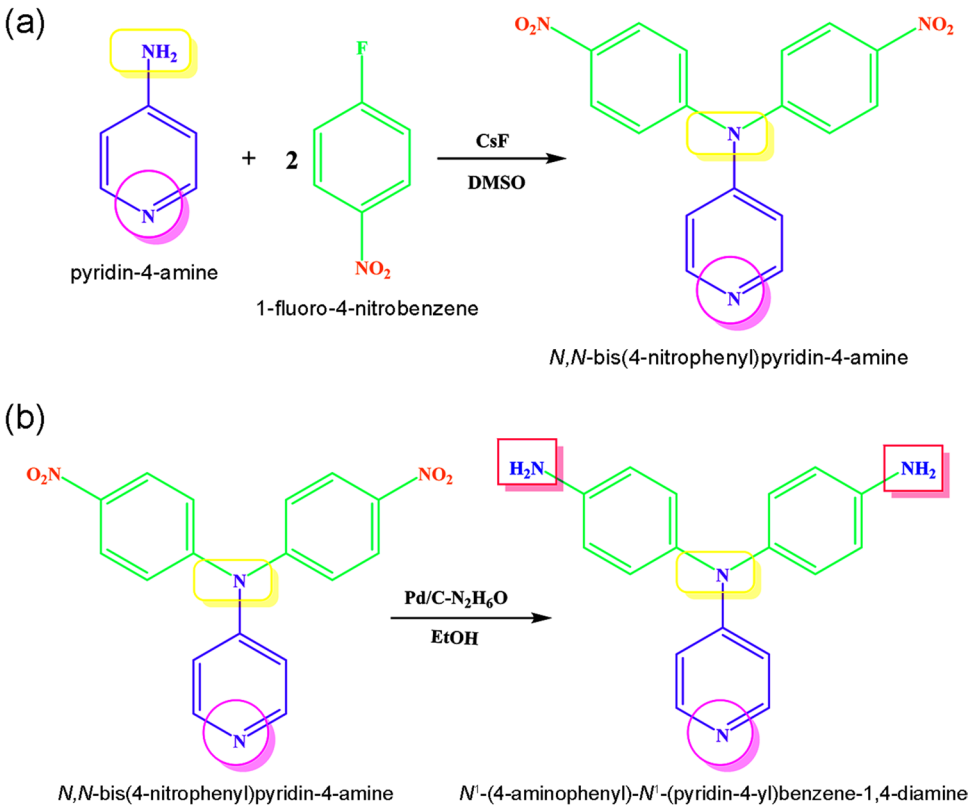
Synthesis of *N,N*-bis(4-nitrophenyl) pyridine-4-amine and *N,N*-bis(4-aminophenyl) pyridine-4-amine

In the fume hood, 1-fluoro-4-nitrobenzene (3.52 g, 25 mmol), cesium fluoride (3.79 g, 25 mmol), and pyridin-4-amine (1.17 g, 12.5 mmol) were weighed into a 3-necked 250 mL glass flask and dissolved in 50 mL of DMSO. The mixture was heated to 110 °C under an argon atmosphere and stirred with a magnetic stirrer for 12 h. After cooling to room temperature, the reaction mixture was precipitated by adding 450 mL of ethanol, and the magnetic stirrer was removed. The precipitate was filtered using filter paper in a Gouch funnel. Following filtration, the product was dried under vacuum. The *N,N*-bis(4-nitrophenyl) pyridin-4-amine was then washed three times with acetic acid and dried under vacuum again (Scheme 1a). ^{1}H NMR (400 MHz, DMSO-d6) δ: 8.38 (d, J = 8.9 Hz, 1H), 8.18 (d, J = 8.7 Hz, 1H), 7.94 (d, J = 7.6 Hz, 1H), 7.82 (d, J = 8.9 Hz, 1H), 7.00 (d, J = 8.8 Hz, 1H), 6.37 (d, J = 7.6 Hz, 1H). ^{13}C NMR (101 MHz, DMSO-d6) δ: 159.43, 155.45, 146.71, 145.42, 141.24, 136.79, 125.39, 122.01, 121.59, 109.78 (Figs. S1 and S2).

Similarly, Pd/C (10%) (0.1 g) was weighed into a 3-necked 250 mL glass flask in the fume hood and dissolved in 80 mL of ethanol (EtOH). Next, 3.36 g (10 mmol) of *N,N*-bis(4-nitrophenyl)pyridin-4-amine was added to the flask. The mixture was heated to the boiling point of ethanol on a magnetic stirrer. During the heating process, 20 mL of ethanol and 1.16 g (30 mmol) of hydrazine monohydrate solution were prepared and added dropwise to the flask. The reaction was stirred for 18 h. After 18 h, the mixture was cooled to room temperature. The Pd/C (10%) was filtered out using filter paper. A rotary evaporator was then used to remove the remaining solvent. Following solvent evaporation, *N,N*-bis(4-aminophenyl)pyridin-4-amine was obtained (Scheme 1B). ^{1}H NMR (400 MHz, DMSO-d6) δ: 8.34 (s, 1H), 8.43–8.15 (m, 2H), 8.20–8.00 (m, 3H), 8.00–7.92 (m, 2H), 7.95–7.84 (m, 1H), 7.84–7.58 (m, 3H), 7.50–7.20 (m, 2H), 7.24–7.07 (m, 2H), 7.07–6.98 (m, 2H), 7.01–6.89 (m, 2H), 6.81 (s, 2H), 6.76–6.57 (m, 7H), 6.43–6.30 (m, 3H), 5.66 (d, J = 8.0 Hz, 1H), 5.46 (s, 2H), 5.36 (s, 1H). ^{13}C NMR (101 MHz, DMSO-d6): δ 159.91, 156.34, 155.75, 148.63, 142.15, 140.20, 138.67, 135.63, 131.76, 126.34, 125.40, 124.99, 124.06, 123.99, 123.19, 121.93, 121.58, 121.42, 114.48, 114.13, 113.94, 113.91, 112.39, 111.56, 109.52 (Figs. S3 and S4).

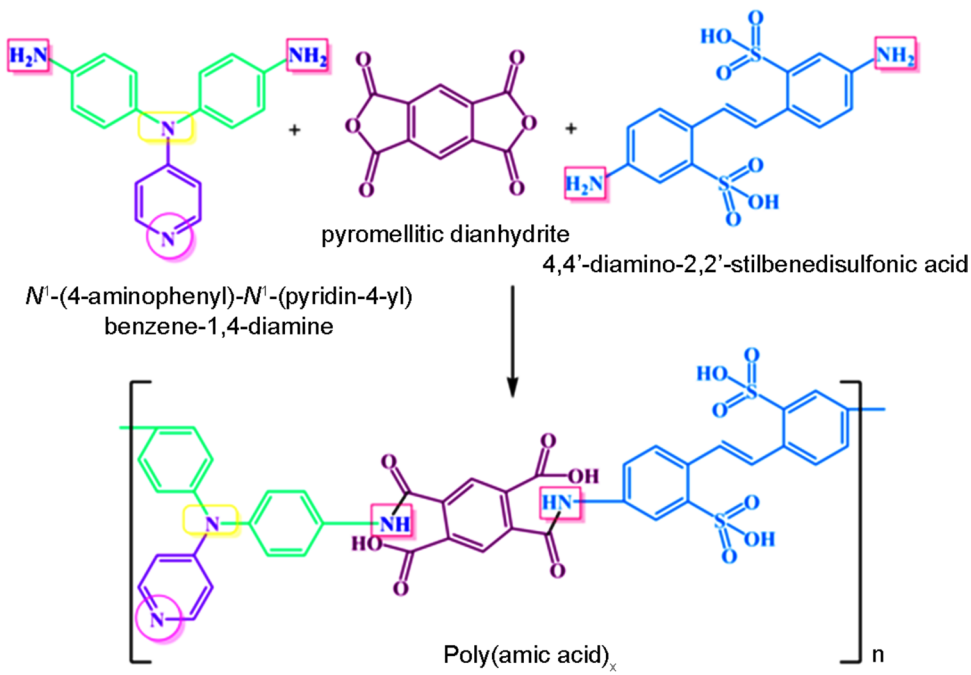
Synthesis of SPI_x with dianhydride and diamine

In the fume cupboard, 0.22 g (0.6 mmol) of 4,4'-diamino-2,2'-stilbenedisulfonic acid and 0.166 g (0.6 mmol) of *N,N*-bis(4-aminophenyl)pyridin-4-amine were weighed into a 250 mL three-necked glass flask under N_2 flow. They were dissolved in 0.4 mL of triethylamine and 6 mL of *m*-cresol, which were carefully added and stirred on a magnetic stirrer at room temperature. The disulfonic acid and diamine dissolved in the mixture. Then, 0.173 g of benzoic acid and 0.261 g (1.2 mmol)

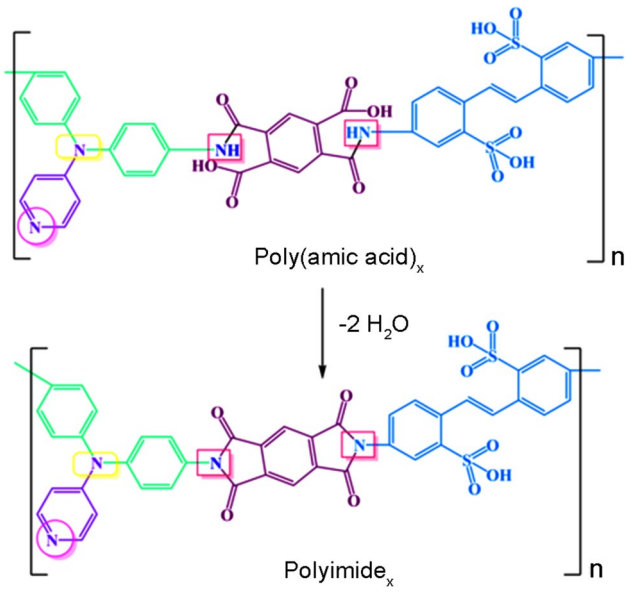


Scheme 1 **a** *N*,*N*-bis(4-nitrophenyl)pyridine-4-amine and **b** *N*,*N*-bis(4-aminophenyl) pyridine-4-amine synthesis schemes

of pyromellitic dianhydride were added. The mixture was stirred at 80 °C for 4 h and then at 180 °C for 24 h to obtain poly(amic acid)$_x$ (PAA)$_x$ (Scheme 2). At the end of the reaction, 10 mL of *m*-cresol was added to dilute the high-viscosity mixture, and the solution was precipitated in ethyl acetate. The precipitated SPI$_x$ was collected using filter paper, washed with acetone, and dried under vacuum at 60 °C for 15 h (Scheme 3). ^{1}H NMR (400 MHz, DMSO-d6) δ 9.21 (s, 1H), 8.27 (s, 1H), 7.81 (s, 3H), 7.55 (s, 1H), 7.03 (t, J = 7.8 Hz, 1H), 6.61–6.51 (m, 3H),



Scheme 2 Poly(amic acid)$_x$ synthesis scheme



Scheme 3 Sulfonated polyimide$_x$ synthesis scheme

3.04 (q, J = 7.2 Hz, 5H), 2.55 (d, J = 5.4 Hz, 1H), 2.32 (d, J = 16.0 Hz, 1H), 2.21 (s, 3H), 1.15 (t, J = 7.2 Hz, 9H).

Results and discussion

FTIR analysis

Testing the exact imidization of SPIs can be very challenging due to their chemical stability [39]. Additionally, PIs are often insoluble in many common solvents [40]. Huang et al. reported that in the FTIR analysis of their sulfonated polyimides, peaks around 704 cm^{-1} and 1766 cm^{-1} were attributed to the symmetric and asymmetric C = O stretching vibrations, respectively. The C-N vibration peak was observed at 1357 cm^{-1}, indicating successful formation of imide rings. Peaks corresponding to the -SO_3H groups were found at 1189, 1106, and 1075 cm^{-1}[41]. In our findings, the completion of the imidization step was confirmed by FTIR. In the spectrum for SPI$_x$, small peak of 1775 cm^{-1} (C = O) and large peak of 1721 cm^{-1} (C = O) are demonstrated. In Fig. 1 the absorptions 1483 cm^{-1} (C–H), 1288 cm^{-1} (C–C), 1229 cm^{-1} (C = C), 1077 cm^{-1} (S = O) sulfonated SPI groups and 1018 cm^{-1} (C-N) are shown.

^{1}H NMR and ^{13}C NMR analysis

^{1}H NMR j values were calculated precisely using the data obtained from the analysis in the MestRaNova (Mnova) program [42]. Li et al. reported that in the ^{1}H NMR spectrum of the.

sc-bSPI-14 membrane they produced, the peaks at 8.79 ppm and 8.61 ppm were attributed to protons in the naphthalene ring attached to the dianhydride. They observed two proton peaks at 8.01 ppm and 7.74 ppm, corresponding to benzene hydrogen atoms in the dianhydride. The chemical shifts at 8.25 ppm, 8.06 ppm, and 7.95 ppm indicated protons derived from sulfonic acid. Benzene hydrogen atoms of triamine were found at 6.56 ppm, 7.62 ppm, 7.60 ppm, and 7.79 ppm. The signals at 6.53 ppm, 7.34 ppm, 7.39 ppm, 7.51 ppm, and 7.64 ppm were attributed to protons from the monomer [43]. Here considering the j values, the resonance peaks in the 1.15–3.04 ppm region represent ethylene, SO_3H and SPI$_x$ protons. Aromatic protons show signals between

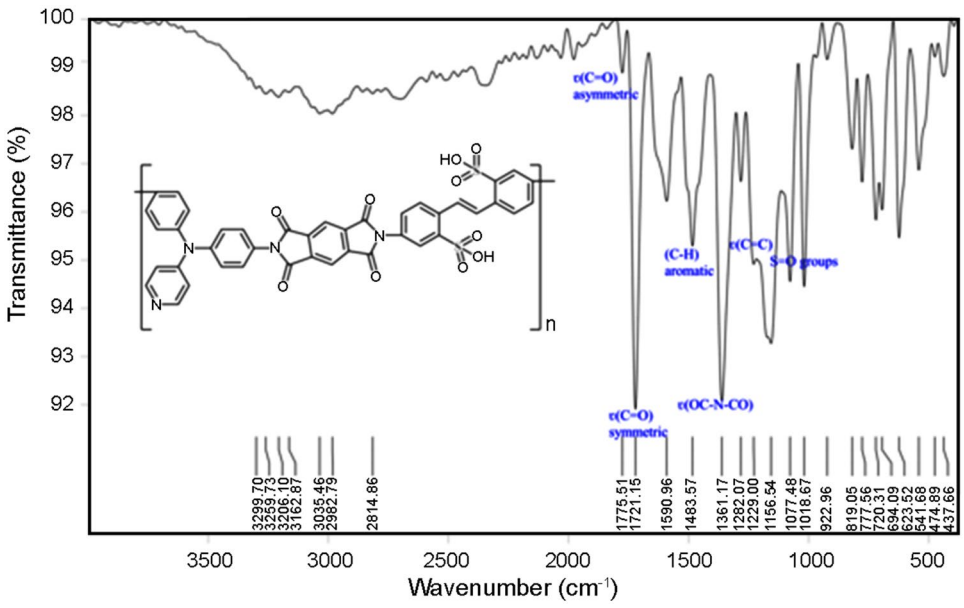


Fig. 1 FTIR spectrum of SPI$_x$

7.81–7.03 ppm. OH proton signals are examined at δ of 9.21–8.27 ppm (Fig. 2). The reasonable attribution of the characteristic peaks further confirms the successful preparation of the SPI_x material.

Since SPI_x is insoluble in THF, determining the molecular weight of the polymer (which is not feasible with GPC) was done using integration values from ^{1}H NMR spectroscopy. The degree of polymerization (DP) of the polymer is calculated by comparing the density of the repeating chain unit (end group) to the proton peak density of a confirmed part of the ^{1}H NMR spectrum (https://www.sigmaaldrich.com/TR/en/technical-documents/technical-article/materials-science- and engineering/polymer-synthesis/polymer-analysis), as shown in Eq. 1:

$$n_x = \frac{ax.my.ny}{ay.mx} \quad (1)$$

Additionally, *nx* can be used in Eq. 2 to multiply the molecular weight (807.77 g.mol^{-1}) of a polymer unit in order to determine the number of repeating units or the degree of polymerization,

$$M_n = nx.Formulawt. \quad (2)$$

In Table 1, the end group peak data from the ^{1}H NMR spectrum of SPI_x are presented. Since the end group peaks are small, nearby peak area values can be used for calculations. The M_n value (M_n 28,300 g.mol^{-1}) obtained from these calculations confirms that SPI_x is a material.

Table 1 Significant ^{1}H NMR data for specification of the molecular weight of SPI_x

SPI_x				
Feature	Moiety	δ (ppm)	Multiplicity	Peak area
End- groups	-NH	2.21	multiplet	2.93*
	$-NH_2$	1.15	singlet	8.67**

*-NH δ (ppm) peak area, **-NH_2 δ (ppm) peak area

UV–Vis analysis

UV–Vis provides structural information about the polymer. The data obtained offer insights into the light absorption properties and is crucial for the characterization of PIs [44]. SPI_x is soluble in DMF, and measurements are taken in this solution. UV–Vis spectroscopy is used to investigate the optical characteristics of SPI_x. This technique provides data related to the polymer's structure and is crucial for understanding SPI formation and validating structural interpretations. SPI_x demonstrates strong absorption in the range of 295–405 nm in solution, which can be attributed to π to π* transitions due to conjugation between nitrogen atoms and aromatic rings. The UV–vis absorption spectra were obtained using SPI_x dissolved in DMF.

Spectra were obtained by preparing solutions with varying concentrations of SPI_x in DMF: 0.01 mL SPI_x + 0.99 mL DMF, 0.02 mL SPI_x + 0.98 mL DMF, 0.03 mL SPI_x + 0.97 mL DMF, 0.04 mL SPI_x + 0.96 mL DMF,

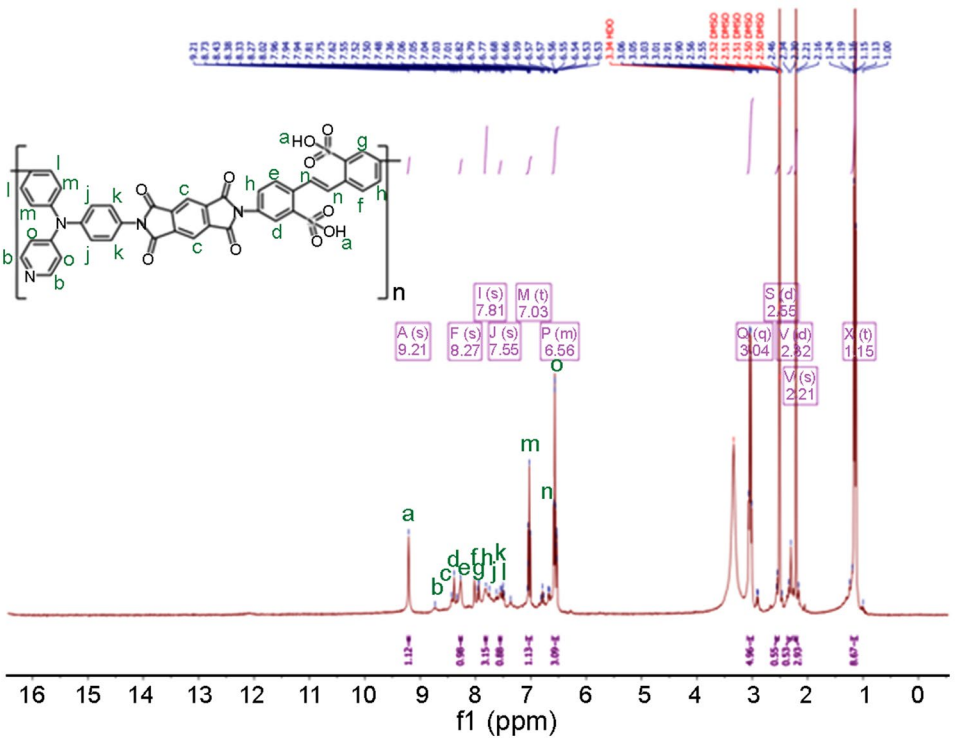


Fig. 2 ^{1}H NMR spectrum of SPI_x

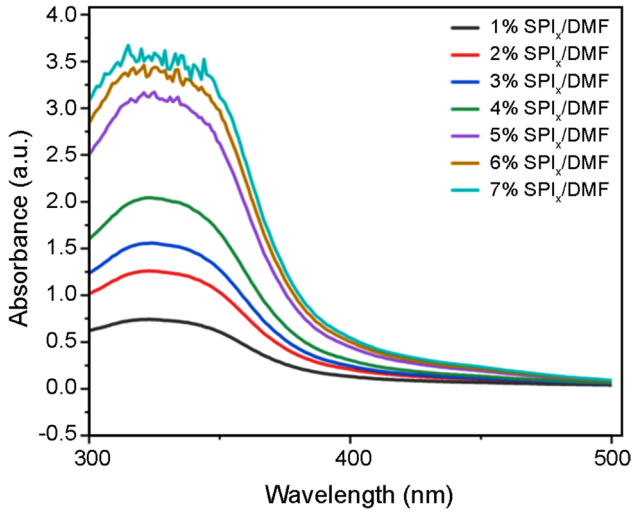


Fig. 3 UV–Vis spectrum of SPI_x

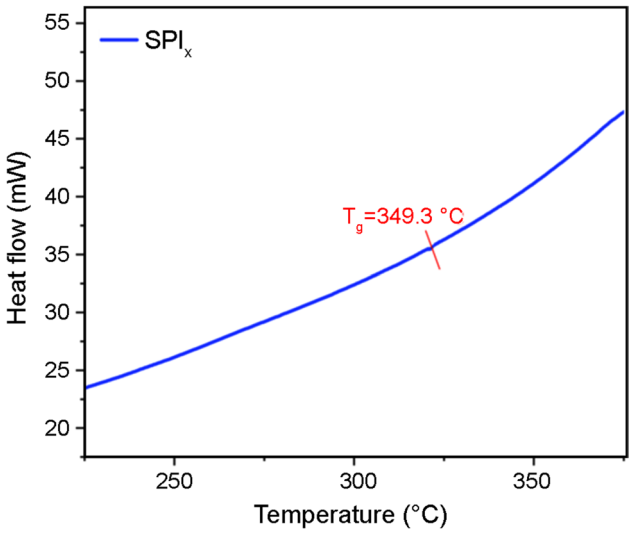


Fig. 4 DSC curve of SPI_x

0.05 mL SPI_x + 0.95 mL DMF, 0.06 mL SPI_x + 0.94 mL DMF, and 0.07 mL SPI_x + 0.93 mL DMF. The UV–vis absorption spectra of these solutions showed an absorbance peak at 310–450 nm. Figure 3 illustrates the UV–vis absorption spectra for different SPI_x concentrations in DMF.

According to Eq. 3 (http://physics.nist.gov/constants), the band gap wavelength of SPI_x is 430 nm, corresponding to an energy gap (Δ) of 2.88 eV.

$$\text{Band} - \text{Gap} = \text{E}(\Delta) = \text{hc}/\lambda_{\max} \quad (3)$$

DSC analysis

DSC is a temperature-dependent technique widely used to detect thermal transitions in polymers. In this investigation, the T_g was clearly identified as an endothermic peak rather than a gradual shift in heat capacity, indicating a distinct thermal transition [45]. Balasubramanian et al. observed that the T_g values of the LSSPI polymers they produced were around 200 °C. They noted that increasing the concentration of the stilbene component did not result in significant changes in the T_g values [46]. In our study, the DSC thermogram data of SPI_x are detailed in Fig. 4. The T_g of SPI_x is determined to be approximately 349.3 °C, as indicated by the heat flow variance in the reverse heat flow. This elevated T_g is attributed to the steric hindrance caused by the pyridine ring, which behaves similarly to an aromatic branched structure within the polymer unit.

TGA/DTA analysis results

The TGA/DTA curve was analyzed in this study. Thermogravimetric data were collected under nitrogen at a heating rate of 5 °C/min. The TGA/DTA thermograms of SPI_x exhibited multiple stages of degradation [47, 48]. Yildiko and Tanriverdi performed a thermal analysis of the sample using TGA/DTA. They observed a two-stage degradation profile for SPI above 200 °C. The TGA thermogram of SPI showed two major degradation steps at approximately 300 °C and 650 °C. The first weight loss between 25 and 140 °C was attributed to the loss of hydrated water from the sulfonic acid groups. The second weight loss between 140 and 200 °C was due to the removal of residual m-cresol solvent. At temperatures above 200 °C, desulfonation occurred up to 400 °C. The first degradation step around 350 °C was associated with the degradation of aromatic sulfonyl groups, while the second step, occurring at temperatures above 450 °C, corresponded to the degradation of the polymer backbone. The DTA curve for SPI revealed peaks at approximately 370 °C, 420 °C, 500 °C, and 590 °C [49]. Figure 5 displays the thermograms with comprehensive data from the TGA and DTA analysis. The first weight loss observed in the SPI_x curves before 130 °C indicates the removal of water absorbed by the highly hygroscopic SO_3 groups. Further weight reduction reflects the elimination of residual m-cresol solvent. The decomposition of sulfonic groups, which results in the release of SO and SO_2 gases up to 450 °C, marks a significant stage in the decomposition process. Degradation peaks as the polymer backbone undergoes breakdown at temperatures exceeding 605 °C.

SEM Analysis

Figures 6, 7, and 8 show the microstructures of SPI_x material produced by our group. The magnification (Mag) dimensions represent different aspect ratios of the original SEM

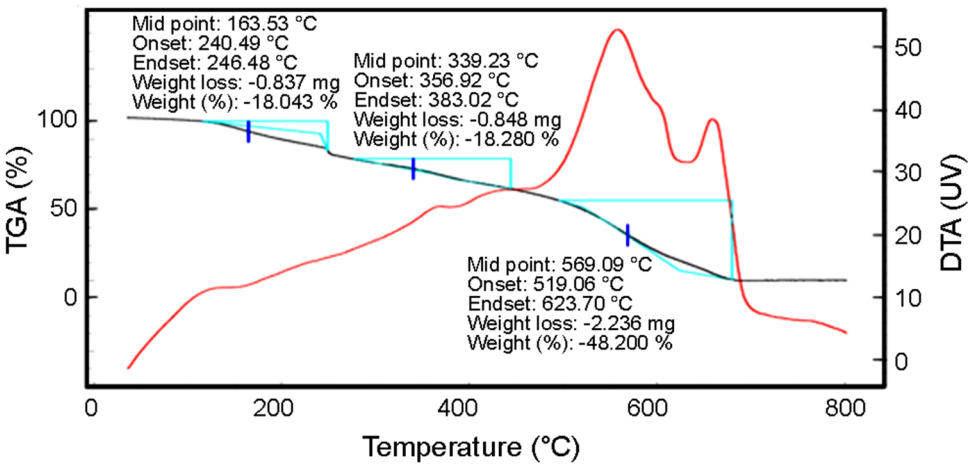


Fig. 5 TGA/DTA curves of SPI_x

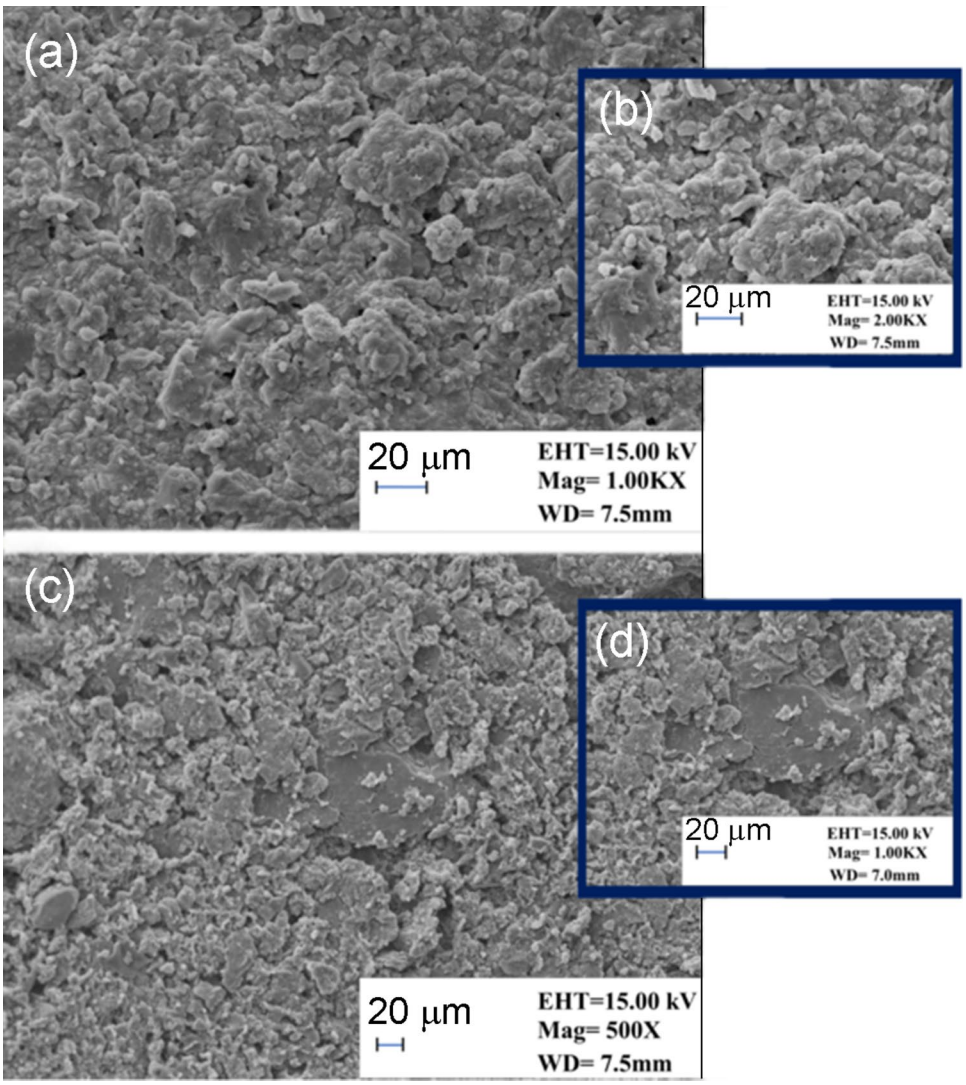


Fig. 6 Surface and cross-section SEM images with 15 kV EHT. Surface and cross-section SEM images with different magnifications for SPI_x in the starting powder: **a** and **b** show 20 µm, 7.5 mm, 1.00 KX and 2.00 KX, **c** and **d** show 20 µm, 7.5 mm and 7.00 mm, 500 X and 1.00 KX

images. The magnifications used are 500X, 1.00 KX, 2.00 KX, 3.00 KX, 5.00 KX, 10.00 KX, and 20.00 KX. For the SEM images analyzed, typical images were selected, with the electron high tension (EHT) recorded at 15 kV. The magnification image widths for this particular analysis are 20 µm, 10 µm, 2 µm, and 1 µm. The working distance (WD)

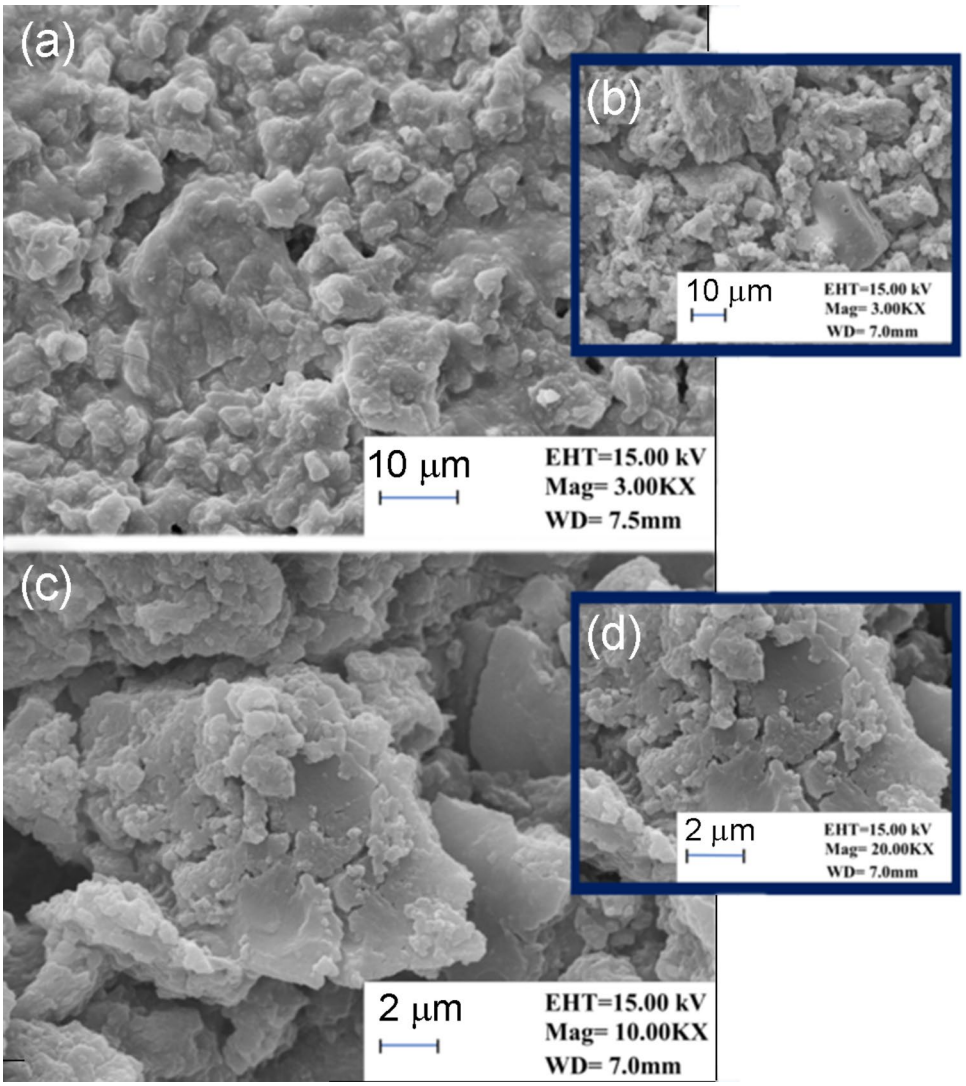


Fig. 7 Surface and cross-section SEM images with 15 kV EHT. Surface and cross-section SEM images with different magnifications for SPI_x in the starting powder: **a** and **b** show 10 µm, 7.5 mm, and 7.00 mm, 3.00 KX, **c**and **d** show 2 µm, 7.00 mm, 10.00 KX, and 20.00 KX

refers to the distance between the bottom of the SEM column and the top of the sample. Within the sample chamber, the sample stage can be positioned closer to the end of the column (short working distance) or further away (long working distance). Here, WD is 7 mm, 7.5 mm, and 8 mm. Figures 6a–d show absolute roughness on the surface at 20 µm magnification; Figs. 7a–d at 10 µm and 2 µm magnifications; and Figs. 8a–d at 20 µm, 10 µm, 2 µm, and 1 µm magnifications. The cross-sectional SEM observations clearly illustrate the coarse and fine structural changes inherent to SPI_x. When comparing the SPI_x 20 µm SEM images with many polyimide samples from the literature, SPI_x exhibits a dense microstructure that closely resembles that of polyimide [50, 51]. SPI_x particles, characterized by their dense microstructure, are predicted to increase porosity in composite films made from this material. The rough surface of SPI_x suggests that composite thick films produced with SPI_x as a starting material may exhibit higher porosity. This increased porosity and surface area can facilitate moisture absorption. In hydration states, SPI_x's proton transfer behavior can vary in the presence of water molecules, which may enhance proton transfer. Therefore, SPI_x appears to be a promising material for cell applications.

DFT studies

It is important to consider the effects of electron interactions in the homomonomer of the non-planar molecule and to use basis sets and polarization functions. Thus, DFT is of major significance in chemistry [52–54].

Geometry optimization

It is important to examine whether the molecule has a symmetrical structure. When a carbon atom is substituted, the carbon bond will determine how the symmetrical geometry of the molecule changes [55, 56]. The optimized geometries of molecules can reveal which atoms protrude from

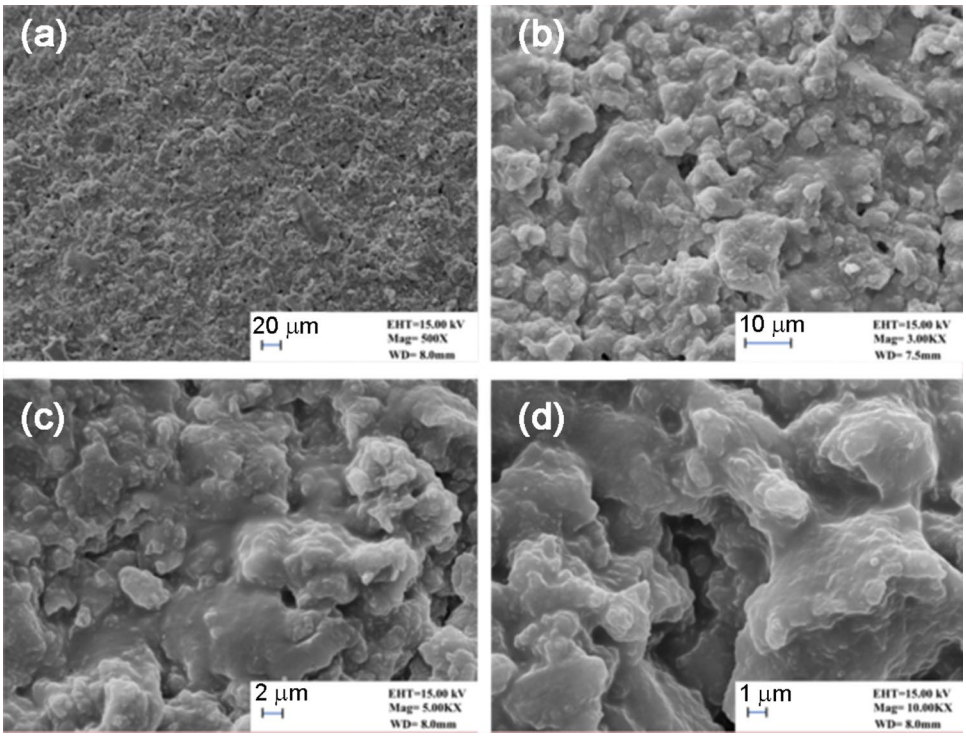


Fig. 8 Surface and cross-section SEM images with 15 kV EHT. Surface and cross-section SEM images with different magnifications for SPI_x in the starting powder: **a** shows 20 µm, 8 mm, and 500 X, **b** shows 10 µm, 7.5 mm, and 3.00 KX, **c** shows 2 µm, 8.00 mm, and 5.00 KX, and **d** shows 1 µm, 8.00 mm, and 10.00 KX

the backbone [57]. Using DFT and TD-DFT methodologies based on condensation polymerization, the optimal ground state structure and total energy conversion of one and three structural units of SPI_x were determined. The optimized bond lengths and bond angles, calculated by the B3LYP method, are listed in Table 2, following the atomic numbering scheme shown in Fig. 9. These values represent the structure with the minimum defined potential energy. For one structural unit, bond lengths range from 1.612 Å to 1.919 Å, while for three structural units, they range from 1.615 Å to 1.915 Å. All bond lengths and bond angles in the phenyl rings are within the expected acceptable values. The C–C bond lengths are between 1.399 Å and 1.408 Å for both one and three structural units, and the C-N bond lengths for N atoms in two separate phenyl groups range from 1.352 Å to 1.433 Å. The C-H bond lengths are between 1.079 Å and 1.081 Å for both one and three structural units, and the C-O bond lengths range from 1.232 Å to 1.248 Å. The C–C-C angles range from 118° to 128°, C-N–C angles from 116° to 124°, and C-S–O angles from 96° to 112°. The dihedral angles for C–C = C-7, C-S–O-H, O = S–O-H, C-N–C-C, C–C-C-H, and C–C-C = C are between 63° and 179° for both one and three structural units.

Dipole moment in DFT system

Electron-donating and electron-accepting groups in molecules defined as π-electron conjugates exhibit asymmetric polarization [58]. Due to the presence of these molecules, they are potential candidates for NLO applications in optical computing and optical signal processing [59]. A molecule to act as NLO must have a large first hyperpolarizability (β) value. In this study, first hyperpolarizability (β), electric dipole moment (μ), and polarizability (Δα) were calculated using DFT and TD-DFT methods [60]. The affinity of SPI_x for NLO behavior at the oligomer level was investigated [61]. Tanriverdi et al. calculated the parameters for one and two structural units of two different polyimides in the gas phase using various basis sets. Their results are as follows: μ (D) = 1.1399, 4.5424, 6.5019, and 6.0111; α (au) = 784.78, 690.30, 1703.6, and 1200.5; β (esu) = 9.4×10^{-35}, 1.5×10^{-34}, 1.6×10^{-35} and 2.4×10^{-35}. This group investigated the NLO behavior of these polyimides by determining β, μ, and Δα using the B3LYP/6-311G and B3PW91/6-311G(d, p) basis sets [61]. In this study, the calculated values are listed in Table 3. The first static β, static μ, and Δα magnitudes from the x, y, and z components were computed [62]. The parameters for one structural unit and two structural units are as follows: μ (D) = 7.001, 2.379, and 7.135; α (au) = 544.9, 735.9, and 2154; β (esu) = 5.9×10^{-35}, 8.8×10^{-35} and 2.9×10^{-35}. The data suggest that these molecules, with their theoretically high polarity values, are promising candidates for nonlinear optical materials.

Table 2 Theoretically gained bond angles (°) and bond lengths (Å) of oligomers of SPI_x

Bond lengths (Å)				Bond angles (°)			
Atomic groups	One structural unit/DFT	One structural unit/TD-DFT	Three structural units/DFT	Atomic groups	One structural unit/DFT	One structural unit/TD-DFT	Three structural units/DFT
C1-C2	1.399	1.406	1.399	C1-C2 = C3	119.36	118.07	119.35
C4 = C5	1.408	1.407	1.408	C4-S15-O18	98.363	97.255	98.927
C7-H61	1.081	1.081	1.081	C4-S15 = O21	112.41	112.79	112.54
C14-S16	1.911	1.913	1.912	C4-S15 = O22	111.34	112.71	110.67
S16-O17	1.846	1.852	1.846	C14-S16-O17	97.645	96.866	97.601
S16 = O19	1.636	1.629	1.615	C14-S16 = O19	112.79	112.93	112.91
S16-O20	1.614	1.620	1.637	C14-S16 = O20	111.92	112.74	112.91
S15-O21	1.637	1.632	1.625	C7 = C8-C9	128.30	128.30	127.74
O17-H67	0.983	0.982	0.983	C2-N23-C27	124.68	124.80	124.72
C2-N23	1.426	1.423	1.426	N23-C27 = O36	125.86	125.73	125.84
C27 = O36	1.232	1.248	1.232	C26-C31-H70	122.42	121.64	122.40
C4-S15	1.914	1.919	1.915	C30-C34 = O39	127.77	129.80	127.87
S15-O18	1.844	1.836	1.842	N33-C32 = O38	126.16	124.43	126.08
S15 = O22	1.612	1.622	1.620	N33 = C35 = C40	120.08	120.87	120.04
O18-H68	0.984	0.982	0.984	C42-N45-C47	121.24	119.80	120.29
C35-N33	1.433	1.408	1.432	C49 = N50-C51	116.69	117.89	116.83
C42 = N45	1.428	1.427	1.431	C46 = C57-H83	119.47	119.69	119.60
C49 = N50	1.352	1.352	1.352	C3-C-4 = C5-C7	177.65	178.82	179.04
C34 = O39	1.233	1.247	1.233	C14-S16-O17-H67	151.59	178.62	151.04
C32 = O38	1.233	1.247	1.233	O22 = S15-O18-H68	109.07	63.059	118.22
C24-O37	1.232	1.247	1.232	C2-N23-C27-C26	179.56	179.65	179.89
C51-N50	1.353	1.352	1.352	C25-C26-C31-H70	179.87	179.91	179.84
C49-H76	1.081	1.079	1.081	C6-C5-C7 = C8	156.32	159.47	159.31

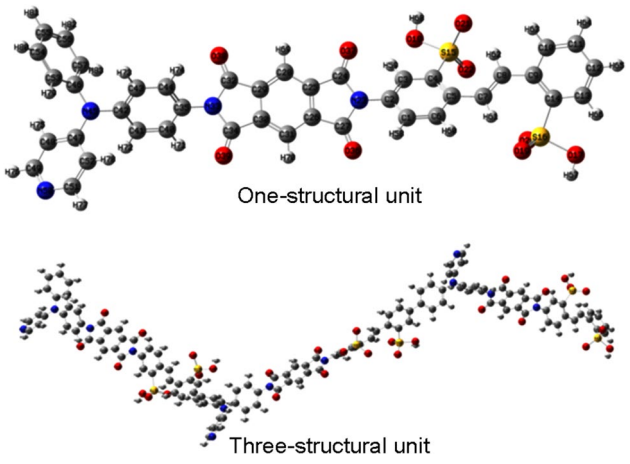


Fig. 9 The view in space of SPI_x (Geometry optimization) one structural unit and three structural units with the 6-311G basis set of DFT/B3LYP method and the 6-311G (d,p) basis set of TD-DFT/B3LYP method

Calculations of *HOMO*–LUMO energies

The ability to donate and accept electrons is described by the HOMO (Highest Occupied Molecular Orbital) and LUMO (Lowest Unoccupied Molecular Orbital) energy levels, respectively [63]. A molecule's optical polarizability, chemical hardness/softness, kinetic stability, and chemical reactivity can all be inferred from the energy difference between its HOMO and LUMO [64]. The negative phase is represented by yellow, whereas the positive phase is depicted in blue. The values for the E_{HOMO} and E_{LUMO} are displayed. By dividing the energy between the HOMO and LUMO, the molecule's reactivity can be determined [65]. Figure 10 in this work displays the volume trajectories of HOMO, LUMO, $HOMO_{-1}$, and $LUMO_{+1}$ for the molecules. Using Table 4, the DFT calculations yielded HOMO = − 5.3904 eV and LUMO = − 3.4504 eV for SPI_x's a structural unit, and HOMO = − 5.4258 eV and LUMO = − 3.4278 eV for SPI_x's three structural units. HOMO = -5.2900 eV and LUMO = − 3.1054 eV values for

Table 3 Polarity (α), static high-order polarity (β), and electric dipole moment (μ) values by DFT study of SPI_x at the levels of the oligomer

Parameters	One structural unit/DFT	One structural unit/TD-DFT	Three structural units/DFT	Parameters	One structural unit/DFT	One structural unit/TD-DFT	Three structural units/DFT
μ_x	− 0.554	− 0.069	− 4.206	β_{XXX}	1238	685.5	− 2663
μ_y	− 3.956	− 2.035	− 4.028	β_{XXY}	− 704.1	− 389.8	1203
μ_z	− 5.750	1.230	− 4.122	β_{XYY}	231.5	315.8	− 128.6
$\mu_{(D)}$	7.001	2.379	7.135	β_{YYY}	− 87.15	− 52.54	− 2550
α_{xx}	− 313.6	− 323.6	− 1239	B_{XXZ}	− 607.8	353.9	− 1074
α_{yy}	− 360.7	− 334.9	− 1038	β_{XYZ}	37.17	90.92	− 1766
α_{zz}	− 354.4	− 350.6	− 1051	β_{YYZ}	5.922	4.389	109.0
α_{xy}	38.38	29.94	− 43.98	β_{XZZ}	− 122.2	− 33.24	283.3
α_{xz}	− 43.80	31.93	220.1	β_{YZZ}	− 4.811	− 8.146	− 826.2
α_{yz}	− 3.152	− 13.60	− 8.010	β_{ZZZ}	− 15.01	25.62	624.2
α(au)	544.9	735.9	2154	β(esu)	5.9×10^{-35}	8.8×10^{-35}	2.9×10^{-35}

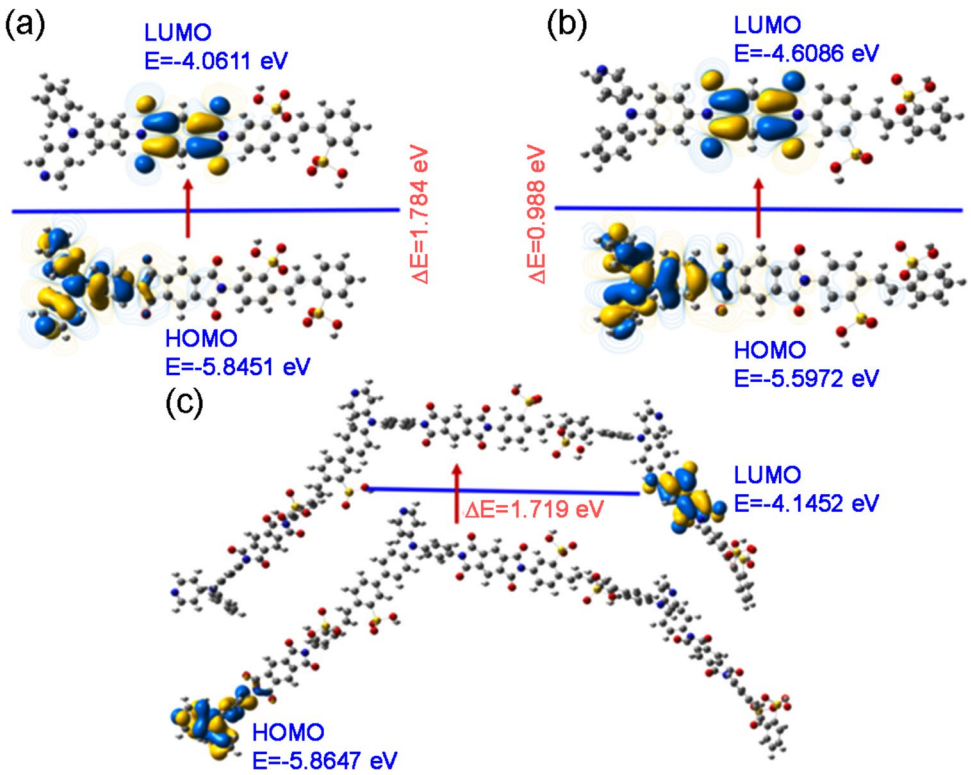


Fig. 10 Images of HOMO–LUMO with one and three structural units of SPI_x: **a** DFT/B3LYP /6-311G basis set of one structural unit, **b** TD-DFT/B3LYP/6-311G (d,p) basis set of one structural unit and **c** DFT/B3LYP /6-311G basis set of three structural units

one structural unit of SPI_x were calculated using TD-DFT. The Energy Gap (Δ) = $|E_{HOMO}—E_{LUMO}|$ between a structural unit and three structural units are 1.784 eV, 0.988 eV, and 1.719 eV, respectively. This suggests the stable existence of both units. Mono-unit and three-unit oligomers have similar energy levels due to similar molecular orbitals with similar atomic orbital compositions. The HOMO level slightly decreased, and the LUMO level modestly increased as the molecule developed. Calculations in quantum chemistry are performed on a single gaseous molecule. Therefore, variations from the observed experimental values may occur when intermolecular interactions are present.

MEP analysis results

The molecular electrostatic potential, V(r), at position r (x, y, z) of the molecule is defined by the energy interaction between the electrons of the molecule [49, 66]. When determining the locations of hydrogen bond interactions

Table 4 Comparison of the energy properties of one structural unit and three structural units of SPI_x

Energy properties	One structural unit/ DFT	One structural unit/ TD-DFT	Three structural units/ DFT
E_{LUMO}	− 3.134	− 2.817	− 3.011
E_{HOMO}	− 5.845	− 5.597	− 5.864
E_{LUMO+1}	− 3.734	− 2.204	− 2.132
E_{HOMO-1}	− 6.843	− 6.750	− 5.989
Energy Gap (Δ) = $\lvert E_{HOMO} - E_{LUMO} \rvert$	2.711	2.780	2.853
Ionization potential ($I = -E_{HOMO}$)	5.845	5.597	5.864
Electron affinity ($A = -E_{LUMO}$)	3.134	2.817	3.011
Chemical hardness ($\eta = (I-A)/2$)	1.355	1.390	1.426
Chemical softness ($s = 1/2\ \eta$)	0.677	0.695	0.713
Chemical potential ($\mu = -(I+A)/2$)	− 4.489	− 4.207	− 4.437
Electronegativity ($\chi = (1+A)/2$)	2.067	1.908	2.005
Electrophilic index ($\omega = \mu^2/2\ \eta$)	13.652	12.300	14.036

and electrophilic and nucleophilic attacks, the MEP is a highly useful tool [67, 68]. It is related to electrical density. The significance of MEP lies in its ability to display the size, shape, and areas of positive, negative, and neutral electrostatic potential of a molecule using a color classification system. This makes it an invaluable tool for studying molecular structure and its physicochemical properties [69]. Different hues correspond to different electrostatic potential values on the surface. The potential levels are color-coded as follows: red, orange, yellow, green, and blue. The range of these maps extends from − 0.03827 a.u. (darkest red) to 0.03827 a.u. (darkest blue). In this case, red denotes the strongest repulsion, while blue denotes the strongest attraction [70]. Typically, only the electronegative atom pairs are linked to negative regions. The map illustrates that areas with positive potential are associated with hydrogen atoms, while regions with negative potential are associated with electronegative atoms, such as oxygen atoms [71]. Typically, only the electronegative atom pairs are linked to negative areas. Here, MEP is utilized to identify vulnerable reactive sites for electrophilic and nucleophilic attacks on one structural unit and two structural units of SPI_x. This was done using the 6-311G (d,p) basis set with the TD-DFT/B3LYP method measured in optimal geometry, and the 6-311G basis set with the DFT/B3LYP method. The hydrogen atom in the structural units shows the strongest positive charge in dark blue (6.442 e^{-2}, 7.245 e^{-2} and 6.558 e^{-2}) according to the MEP map (Fig. 11). Maximum carbon and hydrogen atoms are found in the positive region, indicating suitable sites for nucleophilic attack. Electrophilic reactivity is represented by negative (red) regions (− 6.442 e^{-2}, − 7.245 e^{-2} and − 6.558 e^{-2}). Most of the aromatic ring area is nearly neutral in hue, corresponding to the color green. These findings indicate that the MEP map shows hydrogen atoms with positive potential regions surrounding them, while oxygen atoms have negative potential regions.

Non-linear optical (NLO) analysis results

The D-H···A system's hydrogen bonding can be understood as the donor–acceptor charge displacement between the hydrogen lone pair, thanks to the very useful method known as NBO [72]. The NBO analysis indicates that significant charge transfer energies occur for H-bond interactions between the antibonding σ*(O–H) orbitals and the lone pair (LP) orbitals of O atoms [73]. NBO analysis is a valuable technique for studying charge transfer or hyperconjugative interactions and can be used to investigate both intramolecular and intermolecular binding [74]. Using the second-order perturbation technique, the energies of the hyperconjugation interactions are calculated. Second-order perturbation leads to bonding and antibonding interactions. The NBO technique expresses the perturbation energy as E(2); the higher the value of E(2), the stronger the interaction. In other words, a higher E(2) value indicates greater overall conjugation in the system and a higher propensity for electrons to be donated from donors to acceptors [75]. Here, neutral band orbital energies were computed under the DFT/B3LYP/6311G basis set of a structural unit of SPI_x utilizing the second-order perturbation theory using the Fock matrix approach. Table 5 displays the molecule's natural bond analysis. Here, neutral bond orbital energies were computed under the DFT/B3LYP/6-311G basis set for a structural unit of SPI_x using the second-order perturbation theory with the Fock matrix approach. Table 5 displays the results of the natural bond analysis. The E(2) energy for $\sigma^* \rightarrow \sigma^*$ transitions between S16 and O19 and S16 and O20 is 27.90 kcal mol^{-1}. The E(2) energy for $\sigma \rightarrow \sigma^*$ transitions

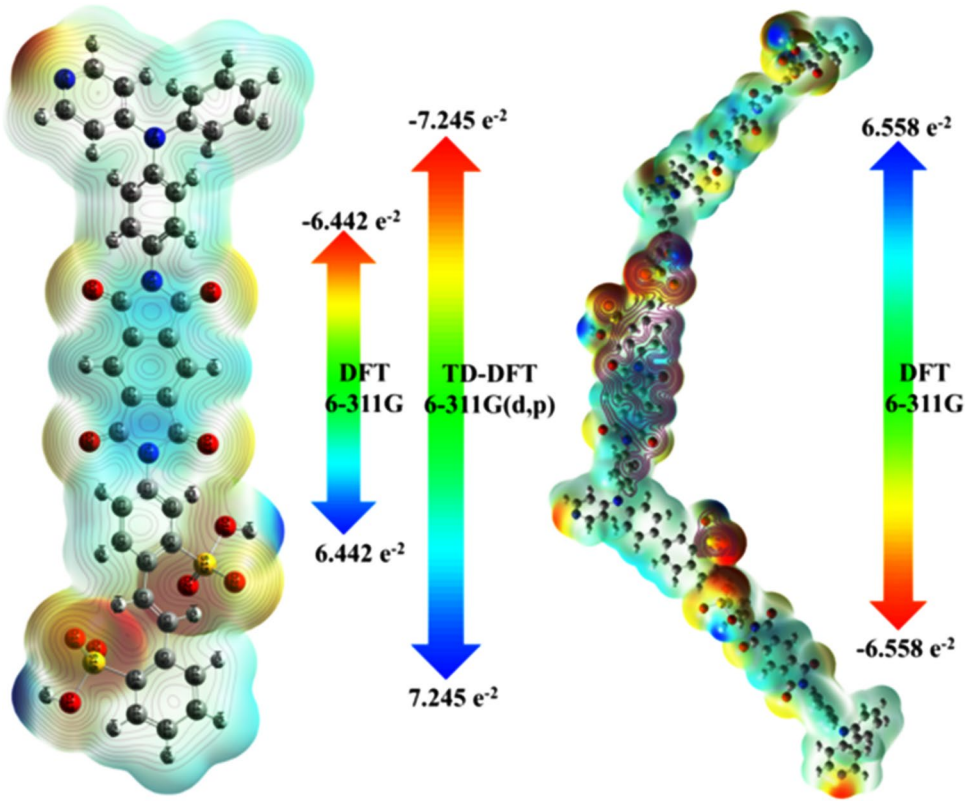


Fig. 11 MEP maps of one structural unit and three structural units of SPI_x one structural unit and three structural units with the 6-311G basis set of DFT/B3LYP method and the 6-311G (d,p) basis set of TD-DFT/B3LYP method

Table 5 σ-σ *, σ*-σ*, π*-π*, π-π* and LP-LP* transitions in natural bond analysis on the 6-311G basis set in the DFT/B3LYP method of a structural unit of SPI_x

Donor NBO (i)	Transitions	Acceptor NBO (j)	E (2) kcal mol^{-1}	E(j)-E(i) a. u	F(i,j) a. u
S15-O18	σ → σ*	S15-O18	9.74	0.47	0.066
S16-O19	σ* → σ*	S16-O20	27.90	0.02	0.050
C1-C2	π → π*	C3-C4	25.47	0.27	0.074
C47-C48	π → π*	C49-N50	29.39	0.27	0.079
C49-N50	π → π*	C51-C52	26.63	0.31	0.081
C3-C4	π* → π*	C5-C6	209.93	0.01	0.078
C9-C14	π* → π*	C12-C13	178.23	0.02	0.080
C47-C48	π* → π*	C51-C52	265.76	0.01	0.078
O18	LP (1) → LP (1)*	H68	27.47	0.83	0.156
O18	LP (2) → LP (1)*	H68	0.76	0.40	0.018
O18	LP(3) → LP (1)*	H68	461.33	0.59	0.469

between S15 and O18 provides the highest energy value at 9.74 $kcal.mol^{-1}$. The E(2) energy for π → π* transitions between C1 and C2 and C3 and C4 is 25.47 $kcal.mol^{-1}$. The E(2) energy for π* → π* transitions between C47 and C48 and C51 and C52 is 265.76 $kcal.mol^{-1}$. The E(2) energy for LP(3) → LP(1)* transitions between O18 and H68 provides the highest energy value at 461.33 $kcal.mol^{-1}$.

QTAIM studies

QTAIM provides a unique approach for dividing molecular properties into regional contributions originating from atoms, which are defined by the zero-flux surfaces of an embedded electron density gradient in real space (https://www.amercrystalassn.org/h-qtaim). The QTAIM approach is a quantum chemical model that characterizes the chemical bonding of a system based on the topology of quantum charge density [76]. Here, a structural unit of SPI_x was calculated using the 6-311G basis set with the DFT/B3LYP method, and parameters were obtained and presented using the QTAIM system. This analysis investigated whether interactions are possible between atoms within the molecule. The results revealed various interactions between closely related O•••H and O•••C atoms. These interactions are shown

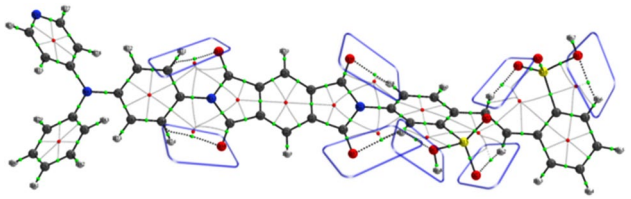


Fig. 12 Topological graph of a structural unit of SPI_x with the 6-311G basis set of DFT/B3LYP method

in Fig. 12 and Table 6. From these findings, it was concluded that the compound is associated with intramolecular interactions arising from hydrogen bonds or electrostatic interactions.

Reduced density gradient (RDG) plots

The non-covalent interaction index (NCI) can be used to examine interactions within the molecule or steric hindrance. In this system, NCI interactions are determined by small values of the RDG [77].

$$RDG(r) = |\nabla\rho(r)|/\rho^{4/3}(r) \tag{4}$$

Table 6 The parameters in r of one structural of SPI_x (all in a.u.)

Interaction	ρ(r)	$\nabla\rho$(r)	$\nabla^2\rho$(r)	G(r)	V(r)	H(r)
O17-H66	+0.019	+0.0099	+0.082	+0.017	− 0.014	− 0.003
O18-H59	+0.019	+0.0024	+0.082	+0.017	− 0.014	− 0.002
O19-H61	+0.018	+0.0015	+0.066	+0.015	− 0.013	− 0.001
O21-H62	+0.018	+0.0017	+0.063	+0.014	− 0.013	− 0.001
O36-H58	+0.012	+0.0032	+0.047	+0.010	− 0.008	− 0.001
O37-H59	+0.012	+0.0080	+0.046	+0.010	− 0.008	− 0.001
O38-C44	+0.010	+0.0012	+0.037	+0.008	− 0.007	− 0.001
O39-C40	+0.010	+0.0039	+0.038	+0.008	− 0.007	− 0.001

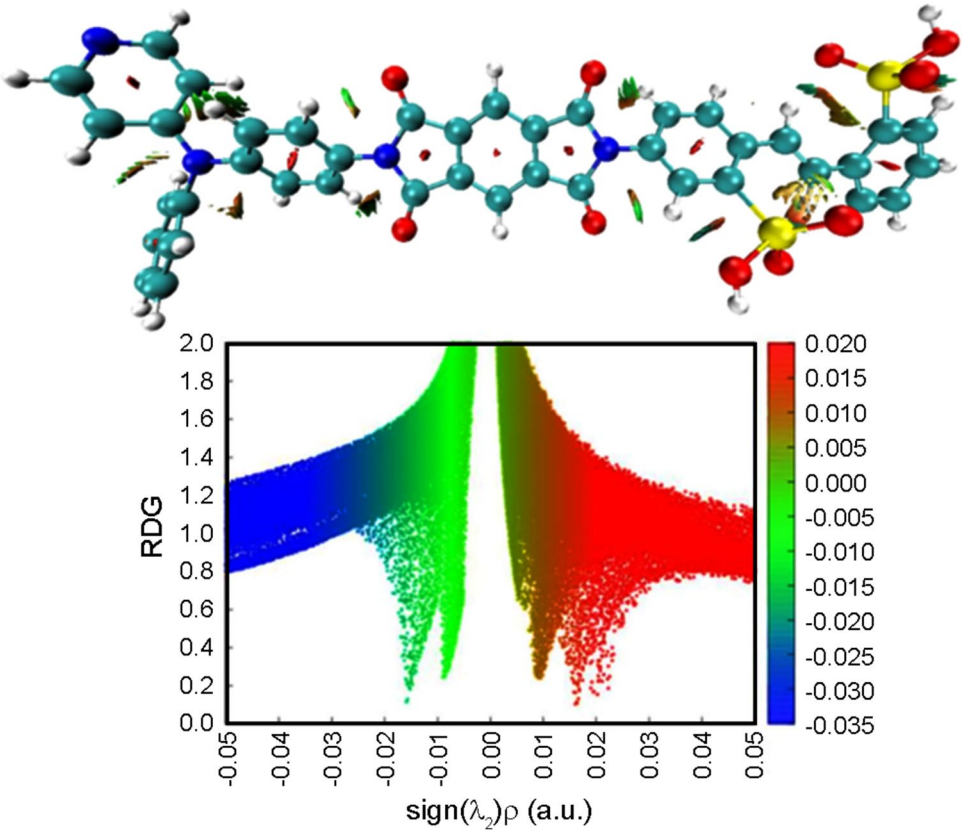


Fig. 13 RDG plots of a structural unit of SPI_x with the 6-311G basis set of DFT/B3LYP method

In Eq. 4, the scatter plots of the RDG are shown in Fig. 13 to describe the different types of interactions. Long et al. produced polyimide but performed RDG studies on small molecules. Specifically, intramolecular weak interactions of TRZ and carbazole segments were also investigated using RDG isosurfaces and scatter diagrams via Multiwfn and Visual Molecular Dynamics (VMD). A noticeable non-covalent weak interaction between TRZ and carbazole segments was observed in RDG isosurfaces (green area in the red dotted box), intuitively indicating the existence of intramolecular TSCT. Furthermore, less intense spikes were observed for TRZ-oCm-HDA than for TRZ-oC-ph in RDG scatter diagrams, indicating weaker CT between TRZ and carbazole segments. This was mainly due to strong steric hindrance effects and a relatively larger donor–acceptor distance in TRZ-oCm-HAD [78]. In the RDG scatter plots, bound interactions (hydrogen bonds or electrostatic bonds), van der Waals interactions, and unbound interactions (steric repulsions) are shown in blue, green, and red, respectively. According to the RDG results, the highest electron density is localized in regions representing hydrogen bonds and electrostatic bond interactions between atoms in the molecule. As seen in Fig. 13, these findings are consistent with the QTAIM results for SPI_x, as the RDG plots were observed in the regions of the dashed bonds.

Electron localized function (ELF)

In the topological graphs of ELF, areas with ELF < 0.5, ELF < 1, and ELF > 0.5 are shown in yellow (or green), dark red (or brown), and white, respectively [79]. Cui et al. presented the local ELF of their fabricated PI-S and PI-SS. The O and S atoms were quite close to each other, which could cause slight overlapping of electron clouds. The overlapping of electron clouds was much more pronounced for O and S atoms in PI-SS. This would lead to the formation of S–O/S=O bonds and charge transfer between them [80]. In our study, regions with extremely low ELF values are shown in blue. The 2D topological ELF graphs of SPI_x are presented in Figs. 14, 15, and 16. The most notable difference observed in the maps is the dense ring and darkness around the S atom, which contains

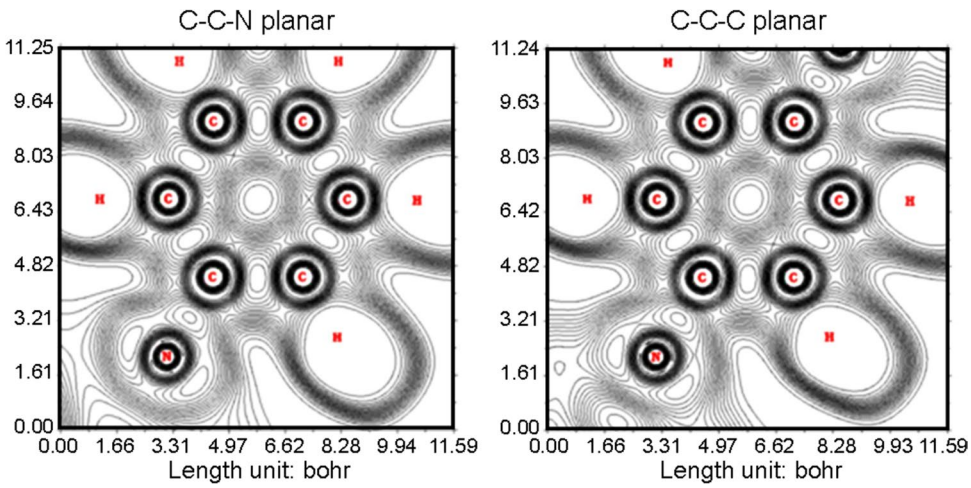


Fig. 14 2D ELF graphics of a structural unit of SPI_x (for C–C-N planar and C–C-C planar) with the 6-311G basis set of DFT/B3LYP method

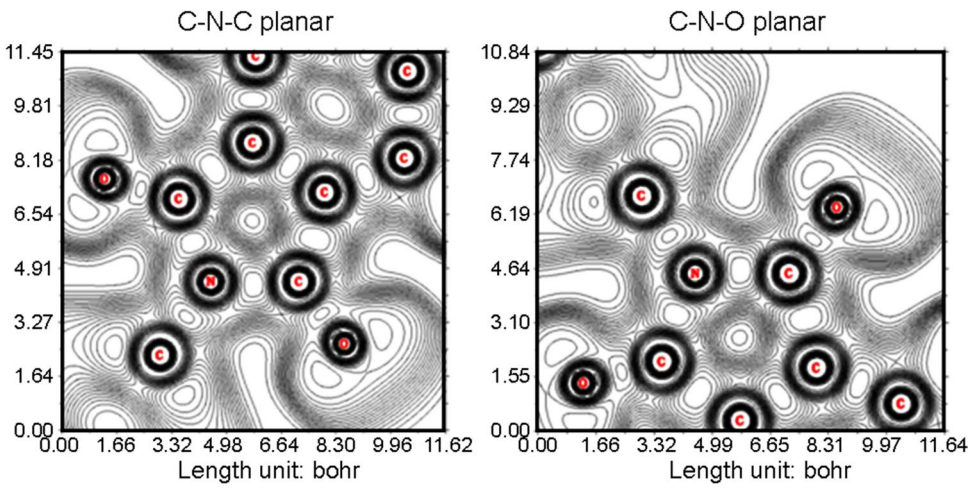


Fig. 15 2D ELF graphics of a structural unit of SPI_x (for C-N–C planar and C-N–O planar) with the 6-311G basis set of DFT/B3LYP method

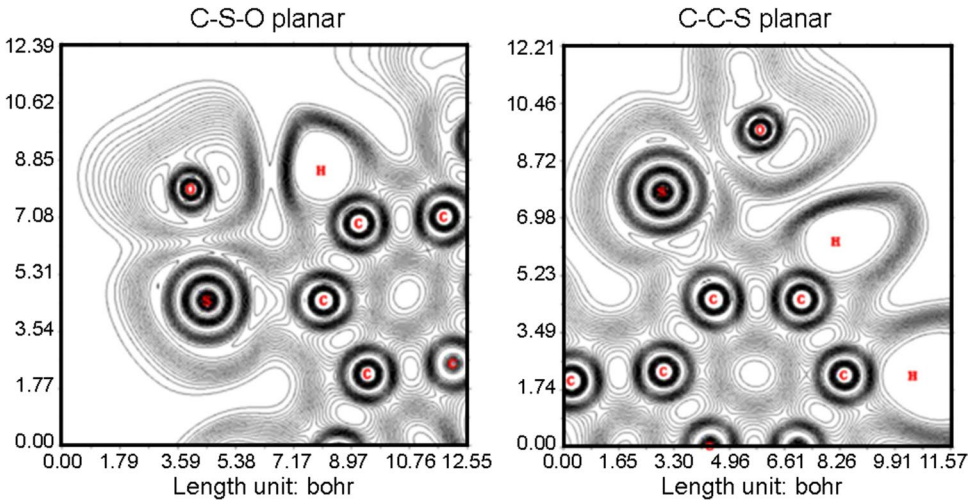


Fig. 16 2D ELF graphics of a structural unit of SPI_x (for C-S–O planar and C–C-S planar) with the 6-311G basis set of DFT/B3LYP method

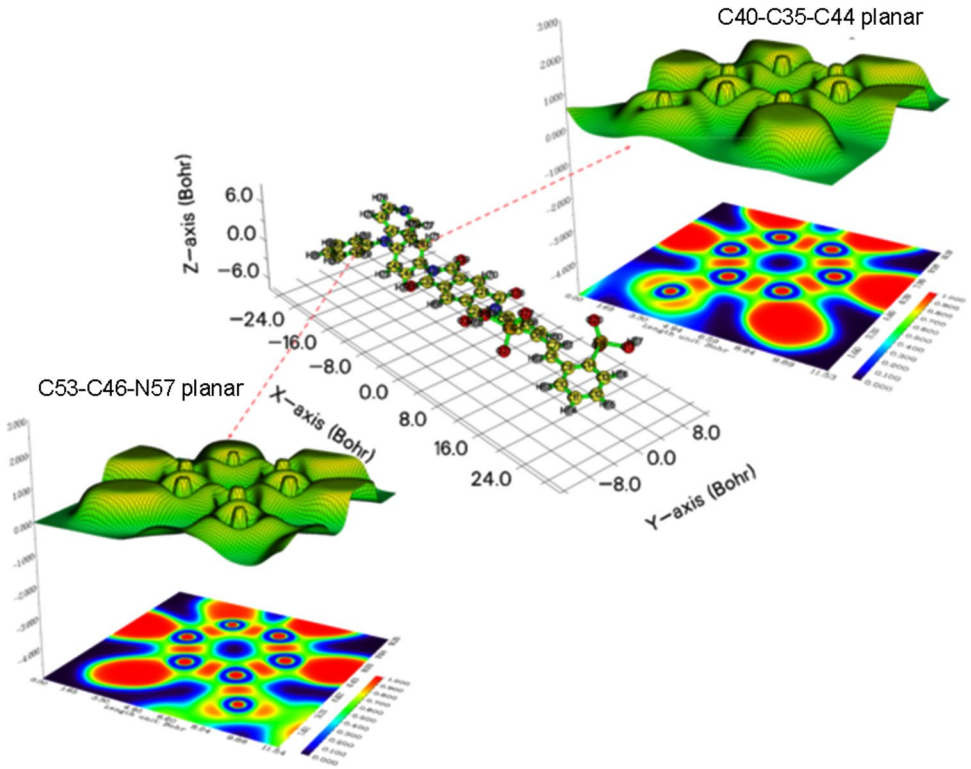


Fig. 17 3D ELF graphics of a structural unit of SPI_x (for C53-C46-N57 planar and C40-C35-C44 planar) with the 6-311G basis set of DFT/B3LYP method

electrons in the 3 s and 3p orbitals of Group 6A. The 3D topological graphs of the ELF are shown in Figs. 17, 18, and 19. C–N–O, C–S–O, and C–C–S planars and their surrounding areas exhibit a significant amount of yellow to green color, indicating greater electron density compared to Figs. 17, 18, and 19. This suggests a situation similar to the ELF of a homogeneous electron gas. The presence of yellow and green colors around the S and O atoms highlights regions where proton transfer can occur. Conversely, the C–C–N, C–C–C, and C–N–C planars and their surrounding areas are depicted in a very intense dark red color, indicating steric hindrances in these regions.

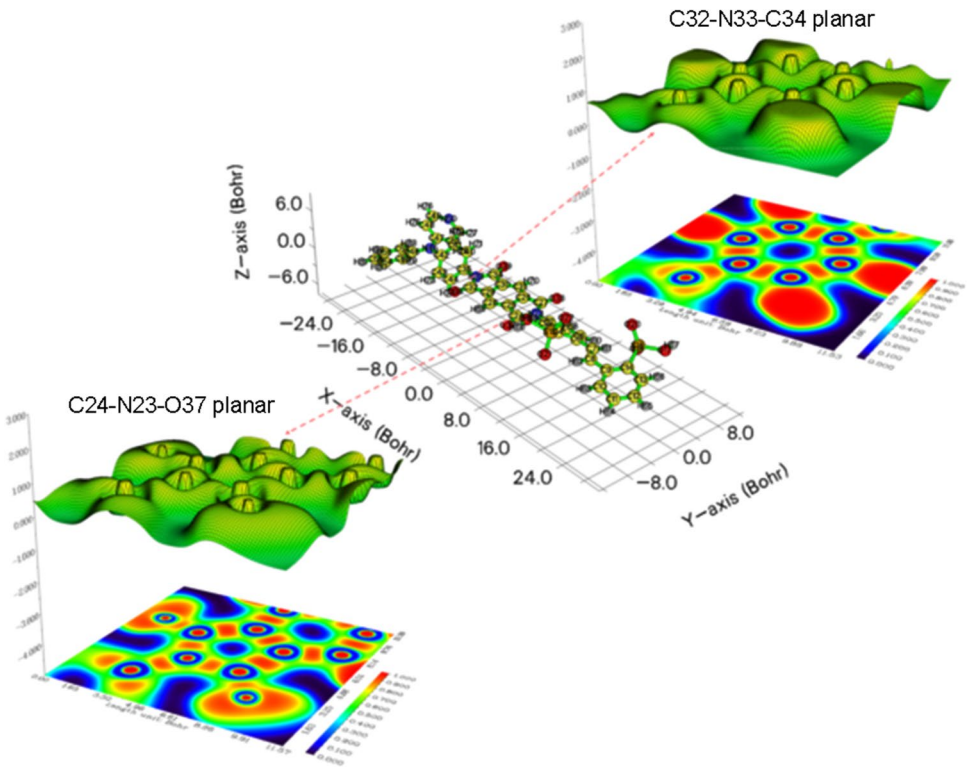


Fig. 18 3D ELF graphics of a structural unit of SPI_x (for C32-N33-C34 planar and C24-N23-O37 planar) with the 6-311G basis set of DFT/B3LYP method

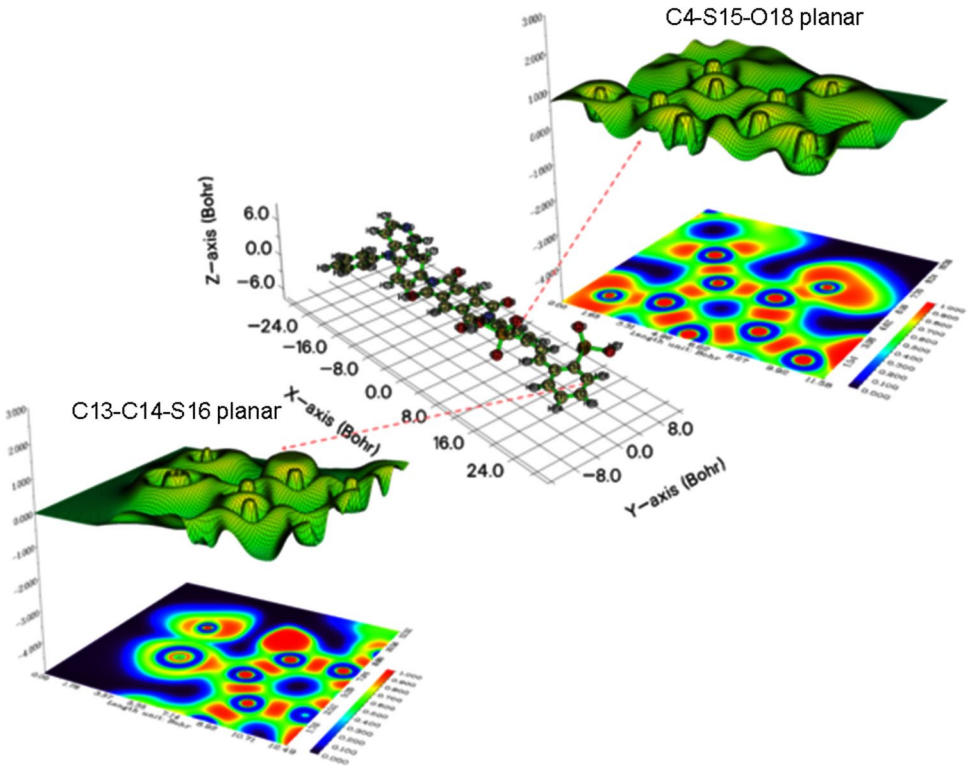


Fig. 19 3D ELF graphics of a structural unit of SPI_x(for C4-S15-O18 planar and C13-C14-S16 planar) with the 6-311G basis set of DFT/B3LYP method

Conclusion

Here, SPI_x was obtained during the continuation of PAA formation. Various characterizations of dinitro, diamine, and SPI_x were performed (^{13}C NMR, ^{1}H NMR, FTIR, UV–vis, DSC, TGA/DTA and SEM). The imidization step was confirmed by FTIR. In the SPI_x spectrum, 1077 cm^{-1} (S = O) and 1018 cm^{-1} (C-N) were observed for the sulfonated SPI groups. In the ^{1}H NMR spectrum, resonance peaks in the region of 1.15–3.04 ppm indicated the presence of SO_3H and SPI_x protons. The OH proton signals were examined at δ of 9.21–8.27 ppm. In the ^{1}H NMR spectrum of SPI_x, the M_n value, determined from the last group peak data, was found to be 28,300 $g.mol^{-1}$, confirming SPI_x as a polymeric material. In the UV–vis absorption spectra of different SPI_x concentrations in DMF, SPI_x exhibited an energy gap (Δ) of 2.88 eV and a wavelength of 430 nm, which was close to the band gap (Δ) values obtained from the E_{HOMO}-E_{LUMO} theoretical calculations. According to the DSC thermogram data of SPI_x and the heat flow variance in the reverse heat flow, T_g was approximately 349.3 °C. The TGA/DTA analysis showed that the decomposition of sulfonic groups, leading to the elimination of SO and SO_2 gases up to 450 °C, marked the beginning of decomposition and was a critical stage. Decomposition peaked when the polymer backbone reached temperatures above 605 °C. SEM showed the microstructures of SPI_x material at 20 µm, 10 µm, 2 µm, and 1 µm, revealing surface roughness. This suggests that, in any composite film case, porosity may increase with film density, and open pores could facilitate moisture absorption. Thus, SPI_x can be considered an alternative material for fuel cell applications, as it allows hydrogen bond interactions and proton transfer between SO_3H and water molecules in hydration states. QTAIM analysis concluded that the structural unit is associated with intramolecular interactions arising from hydrogen bonds or electrostatic bonds.

The bond lengths determined by geometry optimization were 1.612 Å to 1.919 Å for one structural unit and 1.615 Å to 1.915 Å for three structural units. The C–C–C bond angles were between 118° and 128°, the C–N–C angles ranged from 116° to 124°, and the C–S–O angles were between 96° and 112°. Additionally, the dihedral angles of C–C = C–7, C–S–O-H, O = S–O-H, C–N–C–C, C–C–C–H, and C–C–C = C for one structural unit and three structural units ranged from 63° to 179°. The parameter values for one structural unit and two structural units were calculated as μ (D) = 7.001, 2.379, and 7.135 for the gas phase compound; α (au) = 544.9, 735.9, and 2154; β (esu) = 5.9×10^{-35}, 8.8×10^{-35} and 2.9×10^{-35}. Based on these data, they can be considered good candidates for non-linear optical materials. HOMO and LUMO energy values were determined for the single structural unit and three structural units of SPI_x using DFT and TD-DFT calculations. The energy gap (Δ) values between one structural unit and three structural units were 1.784 eV, 0.988 eV, and 1.719 eV, respectively. According to the MEP map, the hydrogen atom in the structural units has the strongest positive charge in dark blue (6.442 e^{-2}, 7.245 e^{-2} and 6.558 e^{-2}). Electrophilic reactivity is represented by negative (red) regions (− 6.442 e^{-2}, − 7.245 e^{-2} and − 6.558 e^{-2}). The map indicates that hydrogen atoms have positive potential regions around them, while oxygen atoms have negative potential regions.

According to the natural bond analysis of SPI_x, the highest energy value of E (2) is 461.33 kcal mol^{-1}, corresponding to LP(3) → LP(1)* transitions between O18 and H68. The RDG results for SPI_x indicate that the highest density of electrons was localized between regions representing hydrogen bonds and electrostatic bonding interactions between the atoms of the molecule, consistent with the QTAIM findings. In the ELF analysis of the SPI_x a structural unit, the C–C-N, C–C-C, and C-N–C planars and the surrounding areas appeared very intense dark red, indicating steric hindrances in these regions. However, the yellow and green colors around the S and O atoms were particularly notable, demonstrating that proton transfer can be achieved in these regions, as also indicated by other theoretical and characteristic analyses.

Supplementary Information The online version contains supplementary material available at https://doi.org/10.1007/s13726-024-01414-6.

Acknowledgements We thank Associate Professor SevdaManap for her help with the IR data. We thank RustemEbiri for his support with the NMR data.

Data availability All other relevant data, including experimental, spectroscopic, thermal and computational data generated and analyzed during this study are included in this article and its supplementary information.

References

1. Mohrmann F, Stoop JA (2019) Airmanship 2.0: innovating aviation human factors forensics to necessarily proactive role. Conference: Future Safety: Has the past become irrelevant? At: The Hague, the Netherlands
2. Millican J, Agarwal S (2021) Plastic pollution: a material problem? Macromolecules. https://doi.org/10.1021/acs.macromol.0c02814
3. Yuanliang J, Wang L, Song Y, Zhu J, Qin M, Wu L, Hu P, Li F, Fang L, Chen C, Hou D (2021) Integrated life cycle assessment for sustainable remediation of contaminated agricultural soil in China. Environ Sci Technol 55:12032–12042
4. Rahmatabadi D, Aberoumand M, Soltanmohammadi K, Soleyman E, Ghasemi I, Baniassadi M, Abrinia K, Bodaghi M, Baghani M (2023) Toughening PVC with biocompatible PCL softeners

for supreme mechanical properties, morphology, shape memory effects, and FFF printability. Macromol Mater Eng 308:2300114
5. Mirasadi K, Rahmatabadi D, Ghasemi I, Khodaei M, Baniassadi M, Baghani M (2024) Investigating the effect of ABS on the mechanical properties, morphology, printability, and 4D printing of PETG-ABS blends. Macromol Mater Eng 309:2400038
6. Ha C-S, Mathews AS (2011) Polyimides and high performance organic polymers. Advanced functional. Springer Berlin Heidelberg, Berlin Heidelberg
7. Ding Y, Hou H, Zhao Y, Zhu Z, Fong H (2016) Electrospun polyimide nanofibers and their applications. Prog Polym Sci 61:67–103
8. Liaw D-J, Liaw B-Y, Yu C-W (2001) Synthesis and characterization of new organosoluble polyimides based on flexible diamine. Polymer 42:5175–5179
9. Chang TC, Wu KH, Chiu YS (1999) Characterization and degradation of some phosphorus-containing polyimides. Polym Degrad Stab 63:103–109
10. Grigoras M, Catanescu C (2007) Imine oligomers and polymers. Polym Rev 44:131–173
11. Zhang X, Kong L, Dai L, Zhang X, Wang Q, Tan Y, Zhang Z (2011) Synthesis, characterization, and thermal properties of poly(siloxane-carborane)s. Polymer 52:4777–4784
12. Castro-Blanco R, Rojas Rodríguez M, Hernández A, Lozano A, Alexandrova L, Aguilar-Lugo C (2020) Aromatic polyimides and copolyimides containing bulky t-butyltriphenylmethane units. Polym Bull 77:5103–5125
13. Ren X, Wang Z, He Z, Yang C, Qi Y, Han S, Chen S, Yu H, Liu J (2023) Synthesis and characterization of organo-soluble polyimides based on polycondensation chemistry of fluorene-containing dianhydride and amide-bridged diamines with good optical transparency and glass transition temperatures over 400 °C. Polymers 15:3549
14. Wu Y, Chen G, Feng C, Yang J (2018) High T_g and thermo-oxidatively stable thermosetting polyimides derived from a carborane-containing diamine. Macromol Rapid Commun 39:e1800484
15. Etemadi H, Afsharkia S, Zinatloo-Ajabshir S, Shokri E (2021) Effect of alumina nanoparticles on the antifouling properties of polycarbonate-polyurethane blend ultrafiltration membrane for water treatment. Polym Sci Eng 61:2364–2375
16. Hosseinzadeh G, Sadeghiazar Sharabiani A, Hermani M, Etemadi H, Shafaati E, Sajjadi SM, Zinatloo-Ajabshir S (2024) Construction of PVC/PVA WO3 3D nanostructure thin film nanocomposite for treatment of oil refinery wastewater. J Polym Environ 32:1879–1891
17. Zinatloo-Ajabshir S, Rakhshani S, Mehrabadi Z, Farsadrooh M, Feizi-Dehnayebi M, Rakhshani S, Dušek M, Eigner V, Rtimi S, Aminabhavi TM (2024) Novel rod-like $[Cu(phen)_2(OAc)]\cdot PF6$ complex for high-performance visible-light-driven photocatalytic degradation of hazardous organic dyes: DFT approach, Hirshfeld and fingerprint plot analysis. J Polym Environ 350:119545
18. Zinatloo-Ajabshir S, Morassaei MS, Salavati-Niasari M (2019) Eco-friendly synthesis of $Nd_2Sn_2O_7$–based nanostructure materials using grape juice as green fuel as photocatalyst for the degradation of erythrosine. Compos Part B-Eng 167:643–653
19. Zinatloo-Ajabshir S, Salavati-Niasari M (2019) Preparation of magnetically retrievable $CoFe_2O_4@SiO_2@Dy_2Ce_2O_7$ nanocomposites as novel photocatalyst for highly efficient degradation of organic contaminants. Compos Part B-Eng 174:106930
20. Rahimpour H, Amini AB, Sharifi F, Fahmi A, Zinatloo-Ajabshir S (2024) Facile fabrication of next-generation sustainable brick and mortar through geopolymerization of construction debris. Sci Rep 14:10914
21. Zinatloo-Ajabshir S, Mahmoudi-Moghaddam H, Amiri M, Akbari Javar H (2024) A green route for the synthesis of sponge-like Pr_6O_{11} nanoparticles and their application for the development of chlorambucil sensor. Measurement 235:114924
22. Zhang D, Wu H, Smith B, Glezakou V-A (2023) Chapter Five - Harness the power of atomistic modeling and deep learning in biofuel separation. Annu Rep Comput Chem 19:121–165
23. Obot I, Macdonald D, Gasem Z (2015) Density functional theory (DFT) as a powerful tool for designing new organic corrosion inhibitors. Part 1: An overview. Corros Sci 99:1–30
24. Bretonnet J-L (2017) Basics of the density functional theory. AIMS Mater Sci 4:1372–1405
25. Abdullah, Tanriverdi AA, Khan AA, Lee S-J, Park JB, Kim YS, Yildiko U, Min K, Alam M (2024) Selenium-substituted conjugated small molecule: synthesis, spectroscopic, computational studies, antioxidant activity, and molecular docking. J Mol Struct 1304:137694
26. Feller D, Dixon DA (2018) Density functional theory and the basis set truncation problem with correlation consistent basis sets: elephant in the room or mouse in the closet? J Phys Chem A 122:2598–2603
27. Orio M, Pantazis DA, Neese F (2009) Density functional theory. Photosynth Res 102:443–453
28. Li J, Terec A, Wang Y, Joshi H, Yunpeng L, Sun H, Stuparu M (2017) π-Conjugated discrete oligomers containing planar and nonplanar aromatic motifs. J Am Chem Soc 139:3089–3094
29. Liu Y, Li Y, Schanze K (2002) Photophysics of π-conjugated oligomers and polymers that contain transition metal complexes. J Photochem Photobiol C: Photochem Rev 3:1–23
30. Li J, Terec A, Wang Y, Joshi H, Lu Y, Sun H, Stuparu MC (2017) π-Conjugated discrete oligomers containing planar and nonplanar aromatic motifs. J Am Chem Soc 139:3089–3094
31. Matta CF, Ayers P, Cook R (2024) The quantum theory of atoms in molecules and electron localization and delocalization. Electr local-delocal matric. Springer International Publishing, Cham
32. Wilson TR, Alexandrova AN, Eberhart ME (2021) Electron density geometry and the quantum theory of atoms in molecules. J Phys Chem A 125:10622–10631
33. Matta CF, Boyd R (2007) The quantum theory of atoms in molecules: From solid state to DNA and drug design. QTAIM. Wiley, NY
34. Vega D, Aray Y, Rodríguez J (2012) C library for topological study of the electronic charge density. J Comput Chem 33:2526–2531
35. Cossard A, Casassa S, Gatti C, Desmarais JK, Erba A (2021) Topology of the electron density and of its laplacian from periodic LCAO calculations on f-electron materials: the case of cesium uranyl chloride. Molecules 26:4227
36. Popov R, Novikov A, Suslonov V, Boyarskiy V (2023) Molecular switching through chalcogen-bond-induced isomerization of binuclear (diaminocarbene)PdII complexes. Inorganics 11:255
37. Prmila MJ, Arul Dhas D, Joe IH, Sreedharan B (2023) Synthesis, structural, spectroscopic, topological, NLO and docking analysis on 4-ethoxy-3-methoxy benzaldehyde: Experimental and theoretical approach. Polycycl Aromat Compd 44:1–27
38. Frisch MJ, Trucks GW, Schlegel HB, Scuseria GE, Robb MA, Cheeseman JR, Scalmani G, Barone V, Petersson GA, Nakatsuji H, Li X, Caricato M, Marenich A, Bloino J, Janesko BG (2016) Gaussian, Inc., Wallingford CT
39. Yildiko U, Tanriverdi AA (2022) A novel sulfonated aromatic polyimide synthesis and characterization: energy calculations, QTAIM simulation study of the hydrated structure of one unit. BKCS 43:822–835
40. Woo Y, Oh S, Kang YS, Jung B (2003) Synthesis and characterization of sulfonated polyimide membranes for direct methanol fuel cell. J MembrSci 220:31–45

41. Huang W, Long J, Li H, Chen L, Li J, Liang Q, Chen X, Yang Z, Song Y, Zhang Y (2024) Investigation of branched sulfonated polyimide membranes containing self-synthesized trianhydride monomer for vanadium flow battery via a combined theoretical-experimental strategy. J Energy Storage 94:112507
42. Claridge T (2009) Software review of MNova: NMR data processing, analysis, and prediction software. J Chem Inf Model 49:1136–1137
43. Li J, Liu J, Xu W, Long J, Huang W, Zhang Y, Chu L (2022) Highly ion-selective sulfonated polyimide membranes with covalent self-crosslinking and branching structures for vanadium redox flow battery. Chem Eng J 437:135414
44. Kumar V, Nasrollahi A, Baliyan V, Park H-S, Lee M-H, Kang S-W (2018) Dual wavelength in situ photoalignment for stable planar alignment of nematic liquid crystals. Opt Mater Express 8:2366
45. Menczel J, Judovits L, Prime R, Bair H, Reading M, Swier S (2008) Differential Scanning Calorimetry (DSC). TAPFA 252:7–239
46. Balasubramanian A, Gunasekaran M, Kannan T (2022) Photo crosslinked stilbene-containing sulfonated polyimide membranes as proton exchange membranes in fuel cell. Eur Polym J 176:111418
47. Osayi J, Iyuke S, Daramola MO, Osifo P, van der Walt I, Ogbeide S (2018) Evaluation of pyrolytic oil from used tires and natural rubber (Hevea brasiliensis). Chem Eng Commun 205:805–821
48. Liu C, Yu J, Sun X, Zhang J, He J (2003) Thermal degradation studies of cyclic olefin copolymers. Polym Degrad Stab 81:197–205
49. Yildiko U, Tanriverdi AA (2021) Synthesis and characterization of pyromellitic dianhydride based sulfonated polyimide: survey of structure properties with DFT and QTAIM. J Polym Res 29:19
50. Kim H-J, Nam S-M (2012) High loading of nanostructured ceramics in polymer composite thick films by aerosol deposition. Nanoscale Res Lett 7:92
51. Zhou J, Sun K, Huang S, He X, Cai W, Zhao Y, Li W (2020) Facile fabrication of polyimide-alumina composite coatings by liquid flame spray. Coat 10:857
52. Torrent-Sucarrat M, Solà M, Duran M, Luis JM, Kirtman B (2003) Basis set and electron correlation effects on ab initio electronic and vibrational nonlinear optical properties of conjugated organic molecules. J Chem Phys 118:711–718
53. Noodleman L, Lovell T, Han WG, Liu T, Torres RA, Himo F (2003) Density functional theory. CC-II, Pergamon, Oxford
54. Solgun DG, Tanriverdi AA, Yildiko U, Ağirtaş MS (2022) Synthesis of axially silicon phthalocyanine substituted with bis-(3,4-dimethoxyphenethoxy) groups, DFT and molecular docking studies. J Incl Phenom Macrocycl Chem 102:851–860
55. Djouama H, Djouama R, MacLeod-Carey D, Nafti N (2024) Geometry optimization and UV/vis spectra of organometallic chalcones functionalized with a benzo-15-crown-5 fragment: A DFT/TD-DFT investigation. Inorg Chim Acta 561:121866
56. Altun K, Yıldıko Ü, Tanrıverdi AA, Cakmak I (2021) Structural and spectral properties of 4-(4-(1-(4-Hydroxyphenyl)-1-phenylethyl) phenoxy) phthalonitrile: Analysis by TD-DFT method, ADME analysis and docking studies. IJCT 5:147–155
57. Khedr AK, Zaky RR, Gomaa EA, Abd El-Hady MN (2022) Elucidation for coordination features of N-(benzothiazol-2-yl)-3-oxo-3-(2-(3-phenylallylidene)hydrazineyl)propanamide on Co^{2+}, $Ni^{2+}$and Cu^{2+}: Structural description, DFT geometry optimization, cyclic voltammetry and biological inspection. J Mol Liq 368:120613
58. Chantzis A, Maroulis G (2011) Interaction-induced electric properties in Kr–Ne from ab initio and DFT calculations. Is there a discrepancy between theory and experiment for the dipole moment? Chem Phys Lett 507:42–47
59. Pluta T, Skrzyński G (2021) Chapter fifteen - time-dependent DFT calculations of the dipole moment and polarizability for excited states. Adv Quantum Chem 83:305–327
60. Paschoal D, Santos H (2016) Computational protocol to predict hyperpolarizabilities of large π-conjugated organic push–pull molecules. Org Electron 28:111–117
61. Tanriverdi AA, Yildiko U, Tekes AT, Cakmak İ, Ata AC (2023) Synthesis, characterization and affinity detection of sulfonated polyimides: confirmation of proton transfer in quantum theory simulations. Polym Bull 80:9853–9880
62. Włodarska M, Mossety-Leszczak B (2021) DFT Studies of selected epoxies with mesogenic units–impact of molecular structure on electro-optical response. Int J Mol Sci 22:3424
63. Vektariene A, Vektaris G, Svoboda J (2009) A theoretical approach to the nucleophilic behavior of benzofused thieno[3,2-b] furans using DFT and HF based reactivity descriptors. ARKIVOC 2009:311–329
64. Xavier S, Periandy S, Ramalingam S (2014) NBO, conformational, NLO, HOMO-LUMO, NMR and electronic spectral study on 1-phenyl-1-propanol by quantum computational methods. Spectrochim Acta Part A: Mol Biomol Spectros 137:306–320
65. Silvarajoo S, Osman M, Kamarudin K, Razali M, Yusoff H, Bhat I, Rozaini MZH, Juahir Y (2020) Dataset of theoretical molecular electrostatic potential (MEP), highest occupied molecular orbital-lowest unoccupied molecular orbital (HOMO-LUMO) band gap and experimental cole-cole plot of 4-(ortho-, meta- and para-fluorophenyl)thiosemicarbazide isomers. Data Brief 32:106299
66. Vetrivel R, Deka RC, Chatterjee A, Kubo M, Broclawik E, Miyamoto A (1996) Studies on the molecular electrostatic potential inside the microporous material and its relevance to their catalytic activity. Theor Comput Chem 3:509–541
67. Murray J, Politzer P (2011) The electrostatic potential: an overview. WIREs Comput Mol Sci 1:153–163
68. Scrocco E, Tomasi J (2007) The electrostatic molecular potential as a tool for the interpretation of molecular properties. Top Curr Chem 42:95–170
69. Gupta VP (2016) Chapter 6-Electron Density Analysis and Electrostatic Potential. PAQC 195–214
70. Akbari Z, Stagno C, Iraci N, Efferth T, Omer EA, Piperno A, Montazerozohori M, Feizi-Dehnayebi M, Micale N (2024) Biological evaluation, DFT, MEP, HOMO-LUMO analysis and ensemble docking studies of Zn(II) complexes of bidentate and tetradentate Schiff base ligands as antileukemia agents. J Mol Struct 1301:137400
71. Lawrence M, Rajesh P, Saral A, Jeyakumar TC, Alharbi NS, Abbas G, Muthu S (2024) Solute solvent interaction study on 9,9-dihydroxynanoic acid by DFT, IR, Raman, UV, MEP, quantum parameters and docking studies. J Mol Liq 397:124053
72. Szatyłowicz H, Jezierska A, Sadlej-Sosnowska N (2016) Correlations of NBO energies of individual hydrogen bonds in nucleic acid base pairs with some QTAIM parameters. Struct Chem 27:367–376
73. Rahmawati S, Radiman C, Martoprawiro M (2018) Density functional theory (DFT) and natural bond orbital (NBO) analysis of intermolecular hydrogen bond interaction in "Phosphorylated Nata De Coco – Water." Indones J Chem 18:173
74. Weinhold F, Landis C, Glendening E (2016) What is NBO analysis and how is it useful? Int Rev Phys Chem 35:399–440
75. Silva D, Daré J, Freitas M (2020) Conformational preferences of fluorine-containing agrochemicals and their implications for lipophilicity prediction. Beilstein J Org Chem 16:2469–2476

76. Popelier P (2022) Non-covalent interactions from a quantum chemical topology perspective. J Mol Model 28:276
77. Lu T, Chen F (2012) Multiwfn: a multifunctional wavefunction analyzer. J Comput Chem 33:580–592
78. Long Y, Chen K, Li C, Wang W, Bian J, Li Y, Liu S, Chi Z, Xu J, Zhang Y (2023) Molecular design strategy for through-space charge transfer blue polyimides with rigid non-conjugated backbone and the role of alicyclic imide linker. Chem Eng J 471:144759
79. Raczyński K, Pihut A, Panek J, Jezierska A (2021) Competition of intra- and intermolecular forces in anthraquinone and its selected derivatives. Molecules 26:3448
80. Cui S, Li T, Tao D, Zhang D, Cao Y, Xu F (2024) Disulfide bonded polyimide cathode of rechargeable magnesium batteries: improved capacity via reversible break/formation of disulfide and sulfur-oxygen bonds. Energy Storage Mater 71:103672

Springer Nature or its licensor (e.g. a society or other partner) holds exclusive rights to this article under a publishing agreement with the author(s) or other rightsholder(s); author self-archiving of the accepted manuscript version of this article is solely governed by the terms of such publishing agreement and applicable law.